



Cite this: *Mater. Adv.*, 2021,
2, 1570

Applications of MXene ($Ti_3C_2T_x$) in photocatalysis: a review

Xing Li, ^a Yang Bai, ^a Xian Shi, ^b Na Su, ^a Gongzhe Nie, ^a Rumeng Zhang, ^c Hongbo Nie ^{ad} and Liqun Ye ^{ae}

MXenes are two-dimensional nanomaterials, which can be constructed from different elements. The rich interlayer groups, surface groups, and the flexible layer spacing of MXenes make them ideal catalysts. Among these, $Ti_3C_2T_x$ has gained particular attention as a photocatalyst for photocatalytic CO_2 reduction reactions (CO₂RR), hydrogen evolution reactions (HER), and photocatalytic degradation reactions. The structure of $Ti_3C_2T_x$, hydrophilic surface functional groups, and the Gibbs free energy for hydrogen adsorption lead to the excellent photocatalytic HER performance of this material. Numerous surface defects on $Ti_3C_2T_x$ also provide plentiful CO_2 adsorption sites for CO₂RR. It is the structure of two-dimensional nanomaterials and their high-speed electron transport channels that enable their excellent catalytic oxidation activity. However, at present, there are still challenges that limit their further application, the most significant of which is the material stability. In order to overcome this, the synthetic routes to prepare these photocatalysts need to be adapted.

Received 30th November 2020,
Accepted 27th January 2021

DOI: 10.1039/d0ma00938e

rsc.li/materials-advances

1 Introduction

Photocatalysis is an environment-friendly technology developed in the 20th century. When light is absorbed by some special semiconductors, namely “photocatalysts”, electrons (e^-) originally in the valence band (VB) are excited to the conduction band (CB) and holes (h^+) are formed in the initial position. Free electrons with strong reducibility can reduce the valence state of some elements in compounds (such as carbon in CO_2 and nitrogen in N_2) when regular methods are not useful or cost too much. Thus far, photocatalysis has shown its huge application prospects in clean energy, environmental remediation, and many other fields; currently, researchers are heading towards new photocatalyst development and reaction mechanisms. Photocatalytic hydrogen evolution reaction (HER), CO_2 reduction reaction (CO₂RR), and photocatalytic degradation reaction represent the three main aspects of photocatalysis.

^a State Key Laboratory of Oil and Gas Reservoir Geology and Exploitation, School of Oil & Natural Gas Engineering, Southwest Petroleum University, Chengdu, 610500, China. E-mail: baiyanghyq@foxmail.com

^b Institute of Fundamental and Frontier Sciences, University of Electronic Science and Technology of China, Chengdu, 610054, China

^c Key Laboratory of Ecological Security for Water Source Region of Mid-line Project of South-to-North Water Diversion of Henan Province, College of Chemistry and Pharmaceutical Engineering, Nanyang Normal University, Nanyang, 473061, China

^d CNOOC (China) Co., LTD. Tianjing Branch, Tianjing, 300452, China

^e College of Materials and Chemical Engineering, Key Laboratory of Inorganic Nonmetallic Crystalline and Energy Conversion Materials, China Three Gorges University, Yichang, 443002, China. E-mail: lqye@ctgu.edu.cn

Photocatalytic nanomaterials have an extensive number of potential applications. When their particle size is below a certain value, the Fermi level of the electronic energy levels morphs from continuous to discrete levels and the energy gap grows wider. These semiconductors are, therefore, more susceptible to photon excitation, which improves their photocatalytic activity.¹

Nanomaterials can be divided into four categories, according to the dimensions of their structural scale: (1) zero-dimensional materials, *e.g.*, groups of nanostructure clusters; (2) one-dimensional nanomaterials, *e.g.*, fibrous nanotubes, nanowires, nanoribbons, or other related structures; (3) two-dimensional nanomaterials, *e.g.*, layered nanomaterials, quantum wells, superlattices, and other structures; (4) three-dimensional nanomaterials, *e.g.*, composite structures consisting of one or more zero-dimensional, one-dimensional, or two-dimensional nanomaterials. The first three are collectively known as low Vannami materials. In low Vannami materials, two-dimensional nanomaterials show significant changes in the surface, electron energy levels, state density, and other aspects compared with three-dimensional materials. This due to the fact that their thickness is greatly reduced compared to other two-dimensional materials; thus, these possess unique optical and electronic characteristics, which make them a hot topic in catalysis.^{2,3}

MXenes are two-dimensional nanomaterials and have a general material formula of $M_{n+1}X_nT_x$. In this formula, M represents nitrogen or carbon, X is generally a transition metal element, and T represents the functional groups. MXenes typically consist of transition metal carbides, nitrides, or carbides that are several



atomic layers thick. It was first reported in 2011⁴ that MXene materials have comparable conductivity towards transition metal carbides due to the presence of hydroxy groups or terminal oxygen species on their surfaces. The most important feature of this range of materials is that, unlike conventional battery materials, they provide more channels for ions to move through, thus dramatically increasing their speed.

$\text{Ti}_3\text{C}_2\text{T}_x$ was the first discovered MXene material and is also the most widely used MXene material in the field of photocatalysis.^{5–7} It was first obtained by etching the Al layer of Ti_3AlC_2 with hydrofluoric acid. In this paper, the application of $\text{Ti}_3\text{C}_2\text{T}_x$ as a photocatalyst and approaches to improve its catalytic performance are summarized.

2 MXene

2.1 From MAX to MXene. MXenes are a type of two-dimensional nanomaterials with covalent bonds formed between the early transition elements and nitrogen or carbon elements. This furnishes an intramolecular skeleton in which the layers are connected by hydrogen bonds. Since the first Mxene, $\text{Ti}_3\text{C}_2\text{T}_x$, was discovered in 2011, more than 20 kinds of MXene materials including M_2X , M_3X_2 , and M_4X_3 have been successively prepared.^{7,8} Due to their unique structure and properties, MXenes have been widely favored for use in battery applications.

The preparation of MXenes can be divided into two approaches, namely, bottom-up and top-down. Presently, the top-down etching method is commonly employed. This is due to the MAX phase^{9,10} (commonly, M means early transition metal elements such as Ti and Nb; A represents the Al or Si layer; X represents C or N elements) as M is mainly composed of metallic bonds between the atoms, which are connected to A. The chemical properties are largely dictated by A. By using certain concentrations of hydrofluoric acid or LiF/HCl¹¹ to etch the MAX phase of Ti_3AlC_2 , ternary carbides within the titanium carbon layers become closer to each other. In this process, the Al layer is etched away gradually, resulting in a greater carbon-titanium interlayer spacing in the $\text{Ti}_3\text{C}_2\text{T}_x$ product. In order to obtain Ti_3AlC_2 with a graphene-like structure consisting of only

a few or single layers, mechanical or chemical intercalation dissection is required. However, when chemical intercalation is used for stripping, some organic molecules may occupy the active sites exposed on the surface, which is unfavorable for photocatalytic reactions.

Etching is a slow process, as shown in Fig. 1(a). In this process, Al layers are gradually peeled off, while the Ti-C skeleton layers are not damaged because of their strong ionic bonding.¹² Free groups such as $-\text{OH}$ and some H_2O molecules enter into the framework of Ti-C and become inter-connected by hydrogen bonds, which expands the layer spacing of $\text{Ti}_3\text{C}_2\text{T}_x$. This permits ions with a large radius to enter the layer spacing,¹³ providing an operating space for the ion intercalation method to peel-off few layers of $\text{Ti}_3\text{C}_2\text{T}_x$. The number of $-\text{OH}$ groups and H_2O molecules within the interlayer space accounts for the large electrical capacity of $\text{Ti}_3\text{C}_2\text{T}_x$.

$\text{Ti}_3\text{C}_2\text{T}_x$ obtained by direct etching with hydrofluoric acid possesses a different morphology to $\text{Ti}_3\text{C}_2\text{T}_x$ obtained by etching with LiF/HCl. Furthermore, NMR spectroscopy revealed a greater number of $-\text{OH}$ and $-\text{F}$ functional groups on the surface of $\text{Ti}_3\text{C}_2\text{T}_x$ etched by hydrofluoric acid, while LiF/HCl etching furnished a material with predominantly $-\text{O}$ functional groups.

2.2 Structure and properties of $\text{Ti}_3\text{C}_2\text{T}_x$

2.2.1 Structure of $\text{Ti}_3\text{C}_2\text{T}_x$. As shown in Fig. 2(a), the structure of $\text{Ti}_3\text{C}_2\text{T}_x$ is comprised of three parts: the intralayer skeleton region, the interlayer region, and the surface terminating groups. In the intramolecular skeleton region, Ti atoms and C atoms are stacked alternately to form ionic bonds, and the skeleton of the entire main structure is formed on this basis. In the interlayer region, it was found through neutron diffraction that the interaction between the layers is established through hydrogen bonding between either O or F atoms on the surface and van der Waals forces between these atoms. The strength of interlayer hydrogen bonding depends not only on the orientation of $-\text{OH}$ relative to the entire sheet but also on the number and distribution of the $-\text{OH}$ groups. When there is water between the layers, it can also participate in hydrogen bonding. In addition, a large number of terminal groups are

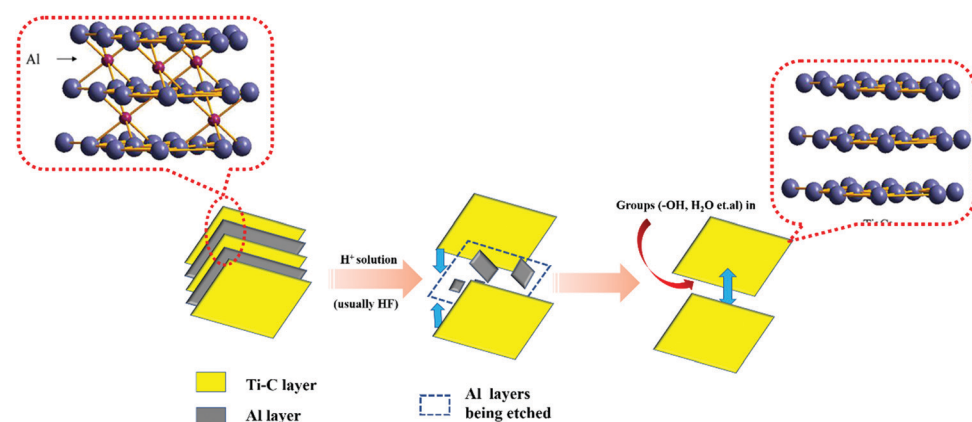


Fig. 1 The process of etching Ti_3AlC_2 to yield Ti_3C_2 .



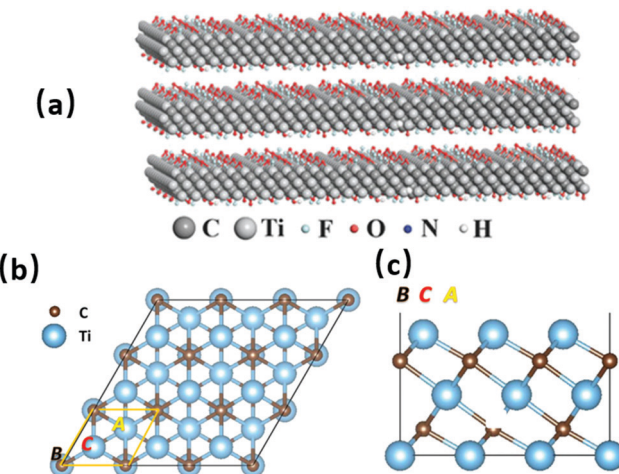


Fig. 2 Schematic diagram showing the crystal structure of Ti_3C_2 (a)¹⁹ and its monolayer with (b) top and (c) side view. The large blue balls represent Ti atoms and the small brown balls represent C atoms. The highlighted unit cell indicates the high symmetry A, B, and C adatom sites.²⁰

randomly distributed on the surface of the $\text{Ti}_3\text{C}_2\text{T}_x$ main structure. These surface groups are directly bonded to the exposed surface and $\text{Ti}_3\text{C}_2\text{T}_x$ is obtained by top-down etching, which mainly includes surface groups such as $-\text{O}$, $-\text{OH}$, and $-\text{F}$. After a period of placement, the $-\text{F}$ groups can be replaced by $-\text{O}$ groups. The surface groups have a great influence on the properties of the $\text{Ti}_3\text{C}_2\text{T}_x$ formed, which can be analyzed by electron energy loss spectroscopy (TEM),^{14,15} neutron scattering,¹⁶ and NMR techniques.^{17,18} These experiments confirm that the surface functional groups of $\text{Ti}_3\text{C}_2\text{T}_x$ are randomly distributed with $-\text{O}$, $-\text{OH}$, and $-\text{F}$ all directly bonded to the surface of the exposed MXene plane. Furthermore, there are no adjacent $-\text{OH}$ functional groups found between the layers. The presence of cations between the layers causes the MXene lamellae to slide easily relative to each other, changing their rheological properties and resulting in their clay-like properties.

2.2.2 Properties of $\text{Ti}_3\text{C}_2\text{T}_x$. The structure of $\text{Ti}_3\text{C}_2\text{T}_x$ determines the electric storage performance. As $\text{Ti}_3\text{C}_2\text{T}_x$ has a wide spacing between the layers, the ions can travel through the layers at a high speed, whilst the hydroxyl or terminal oxygen groups on the surface furnish a material with excellent conductivity. Both factors are important for the use of these MXene materials in batteries.^{20–25}

Various surface groups (such as $-\text{O}$, $-\text{F}$, and $-\text{OH}$) have supplied abundant anchored sites for the base photocatalyst to form efficient heterojunction structures, which are ideal for photocatalytic activities.²⁶ There is also a large number of exposed metal sites on the surface, which can be used as active sites for reactions.

The surface chemical state of MXene materials has a large influence on the regulation of its physical properties. When $-\text{F}$ on the surface is replaced by an $-\text{O}$ group, the electrochemical performance is improved. For example, when $\text{Ti}_3\text{C}_2\text{T}_x$ is treated with a KOH and CH_3OOK solution, the $-\text{O}$ groups on the surface increase, along with the electric capacity. Under an

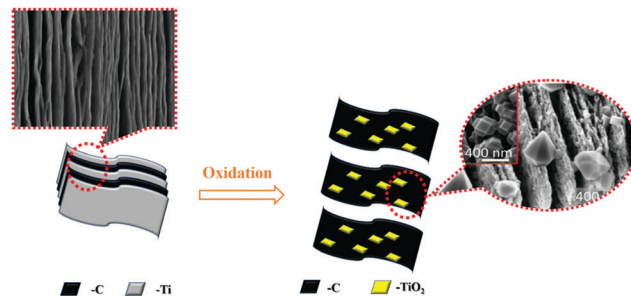


Fig. 3 Oxidation process of $\text{Ti}_3\text{C}_2\text{T}_x$.

atmosphere of N_2 , Ar , or other inert gases, the number of $-\text{F}$ groups on the surface of $\text{Ti}_3\text{C}_2\text{T}_x$ is reduced, after which the electrical capacity is greatly increased.

$\text{Ti}_3\text{C}_2\text{T}_x$ shows an excellent absorption of light between 300 nm and 500 nm.²⁷ Recently, researchers have even found that the absorption can be broadened to the near-infrared (NIR) region. According to a further study, this may be related to its surface plasmon resonance (SPR), and the thinner the material, the stronger the SPR.²⁸ Such a peculiarity makes $\text{Ti}_3\text{C}_2\text{T}_x$ an ideal photothermal co-catalyst.

2.2.3 Instability of $\text{Ti}_3\text{C}_2\text{T}_x$. MXenes typically have poor stability. $\text{Ti}_3\text{C}_2\text{T}_x$ is rapidly oxidized when heated under CO_2 , air, and other environments, and when the surface groups are all $-\text{O}$, $\text{Ti}_3\text{C}_2\text{O}_2$ exhibits metallic properties.^{29,30} $\text{Ti}_3\text{C}_2\text{T}_x$ is also slowly oxidized when exposed to air under atmospheric conditions. After oxidation, $\text{Ti}_3\text{C}_2\text{T}_x$ is called oxidized MXene (denoted as MO).

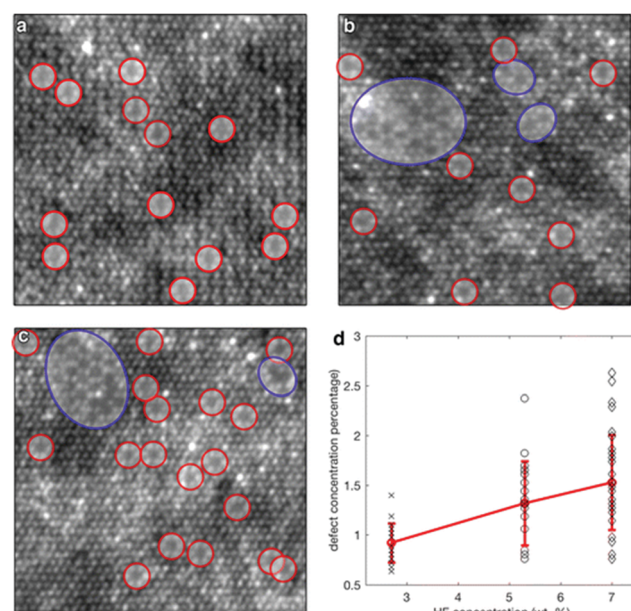


Fig. 4 HAADF-STEM images from single-layer $\text{Ti}_3\text{C}_2\text{T}_x$ MXene flakes prepared using etchants with different HF concentrations: (a) 2.7 wt% HF, (b) 5.3 wt% HF, and (c) 7 wt% HF. Single V_{Ti} vacancies are indicated by the red circles, while vacancy clusters $\text{V}_{\text{Ti}}^{\text{C}}$ are shown by the blue circles. (d) Scatter plot of the defect concentration from the images acquired from samples produced using different HF concentrations. The red line shows the error plot with the average and standard deviation for different HF concentrations.³³

Table 1 Comparison of photocatalysts including $Ti_3C_2T_x$ in HER

Name	H_2 production ($\mu\text{mol h}^{-1}$ g _{catalyst} ⁻¹)	AQY (%)	Activity improvement factor	Sacrificial reagent	Preparation methods	Monolayer or multilayer	Light source	Morphology	Year Ref.
CdS/Ti ₃ C ₂ T _x	14.342	40.1%	(420 nm) 135.59 times	Lactic acid (17.6%)	One-step hydrothermal method	Ti ₃ C ₂ T _x NPs	300 W Xe lamp ($\lambda > 420$ nm)	Cauliflower-structure by self-assembly of many NPs	2017 30
2D-Layered Carbon/TiO ₂	480.8	1.98%	(400 nm)	TEOA (10%)	Ti ₃ C ₂ T _x oxidation	Multilayer	300 W Xe lamp ($\lambda > 400$ nm)	Nanosheets	2017 44
Ti ₃ C ₂ T _x /rutile TiO ₂	17.8	0.3%	Approximately 4 times	Methanol (25%)	Hydrothermal method	Multilayer	200 W Hg lamp ($\lambda > 400$ nm)	2D sheet with TiO ₂ attached on the surfaces and between the sheets	2016 45
Ti ₃ C ₂ /Pt/g-C ₃ N ₄	5000	3.1%	(420 nm) 15 times than pristine g-C ₃ N ₄	TEOA (10%)	Hydrothermal and photodeposition method	Monolayer	300 W Xe lamp porous Nanosheets with nanoparticles	2018 46	
Sulfur-doped Carbon/TiO ₂	333	7.36%		Methanol (10%)	Ti ₃ C ₂ T _x oxidation	Multilayer	300 W Xe lamp ($\lambda > 400$ nm)	Nanosheets	2018 47
Ti ₃ C ₂ T _x /TiO ₂ nanoflowers	783.11	5.86	(350 nm) 6 times	Methanol (20%)	Hydrothermal and calcination	Multilayer	300 W Xe lamp	Nanoflowers	2018 48
Zn ₂ In ₂ S ₃ /Ti ₃ C ₂ T _x	2596.76	8.96%	(420 nm) 1.97 times	0.25 M Na ₂ SO ₃ /H ₂ PtCl ₆	Hydrothermal	Multilayer	300 W Xe lamp ($\lambda > 400$ nm)	Flower-like microspheres	2018 49
d-Ti ₃ C ₂ /TiO ₂ /g-C ₃ N ₄	1620	4.16%	(420 nm) 12.15 times than pure g-C ₃ N ₄ 4 times	TEOA (10%)	Calcination	Monolayer	300 W Xe lamp ($\lambda > 420$ nm)	2D-2D nanosheets	2018 50
ZnS/Ti ₃ C ₂	502.6	35.6%	(429 nm) 6.68 times	Lactic acid (20%)	Hydrothermal	Multilayer	300 W Xe lamp ($\lambda > 420$ nm)	2D-2D nanosheets	2019 51
1D CdS nanorod/2D Ti ₃ C ₂ MXene nanosheet/TiO ₂ nanofibers/MXene	2407	3.8 times than TiO ₂ nanofibers	Methanol (10%)	Electrostatic self-assembly	Monolayer	300 W Xe lamp ($\lambda > 420$ nm)	Sphere-like structure	2019 52	
TiO ₂ nanoparticle/monolayer Ti ₃ C ₂	2650	15.8%	(305 nm) 2.88 times than TiO ₂ nanoparticles/multilayer Ti ₃ C ₂ 2.33 times	Methanol (25%)	Electrostatic self-assembly technique	Monolayer	300 W Xe lamp ($\lambda > 420$ nm)	Nanofibers/nanosheets	2019 53
MoS ₂ /Ti ₃ C ₂	6144.7	1.8 times than O-doped g-C ₃ N ₄	TEOA	Hydrothermal	Multilayer	300 W Xe lamp ($\lambda > 420$ nm)	Spheres-like structure	2019 55	
Ti ₃ C ₂ MXene/O-doped g-C ₃ N ₄	25124	17.59% (405 nm)	0.25 M Na ₂ SO ₃ and 0.35 M Na ₂ S	Electrostatic self-assembly technique	Multilayer	300 W Xe lamp ($\lambda > 400$ nm)	2D nanosheets structure	2019 56	
CdLa ₂ S ₄ /Ti ₃ C ₂	11182.4	15.60% (420 nm)	TEOA (15%)	Hydrothermal	Monolayer	300 W Xe lamp ($\lambda > 420$ nm)	Particle-like structure	2019 57	
Ti ₃ C ₂ MXene quantum dots/g-C ₃ N ₄ Mo _x S@TiO ₂ @Ti ₃ C ₂	5111.8	3.654%	25.97 times	Deposition	Ti ₃ C ₂ MXene quantum dots	300 W Xe lamp Nanosheets		2019 58	
Ti ₃ C ₂ porous MOFs (UiO-66-NH ₂) C-TiO ₂ /g-C ₃ N ₄	204	7.535%	5.99 times than Mo _x S@TiO ₂ @Ti ₃ C ₂ Approximately 8 times	TEOA	In situ growth and hydrothermal	300 W Xe lamp Nanosheets		2019 59	
	1409	8 times than C-TiO ₂	0.1 M Na ₂ S and 0.1 M Na ₂ SO ₃	Calcination	Monolayer	350 W Xe lamp	3D structure	2019 60	
			TEOA (10%)		Multilayer	300 W Xe lamp ($\lambda > 420$ nm)	Smooth sheet-like structure	2019 32	



Table 1 (continued)

Name	H ₂ production (μmol h ⁻¹ g _{catalyst} ⁻¹)	AQY (%)	Activity improvement factor	Sacrificial reagent	Preparation methods	Monolayer or multilayer	Light source	Morphology	Year Ref.
CdS@Ti ₃ C ₂ @CoO	134.46		1.75 times than CdS@CoO		Calcination	Monolayer	300 W Xe lamp	Spheres-like	2019 61
TiO ₂ -Ti ₃ C ₂ -CoS _x	950		5.8 times than TiO ₂	Methanol (20%)	Hydrothermal	Multilayer	300 W Xe lamp (λ > 420 nm)	structure	2019 62
Ti ₃ C ₂ (TiO ₂)@CdS/MoS ₂	8470		3.76 times than CdS/MoS ₂	lactic acid (20%)	Hydrothermal	Multilayer	300 W Xe lamp (λ > 420 nm)	Smooth round block morphology	2019 63
Ti ₃ C ₂ MXene/MoS ₂ nanosheets/TiO ₂ nanosheets	6425.297	4.61%	7.15 times than TiO ₂ /Ti ₃ C ₂ TEOA	Ti ₃ C ₂ T _x oxidation		Multilayer	300 W Xe lamp	Ti ₃ C ₂ nanosheets with MoS ₂	2019 64
2D/3D g-C ₃ N ₄ /Ti ₃ C ₂ (MXene) heterojunction Au/MoS ₂ /Ti ₃ C ₂	116.2		6.64 times	TEOA (10%)	Calcination	Multilayer	300 W Xe lamp (λ > 420 nm)	Nanoparticles	2020 65
2D/2D Ti ₃ C ₂ /g-C ₃ N ₄	72.3	0.81% (400 nm)	10.18 times than pure g-C ₃ N ₄	TEOA (10%)	Electrostatic self-assembly technique	Multilayer	300 W Xe lamp (λ > 420 nm)	Nanosphere-like	2020 66
MXene@Au@CdS	17070.43		1.85 times than pure CdS and 0.25 mol L ⁻¹ Na ₂ SO ₃ solution	0.35 mol L ⁻¹ Na ₂ S TEOA (25%)	Hydrothermal	Monolayer	200 W Hg lamp (λ > 420 nm)	Flat irregularly shaped nanosheets of 2D/2D structures	2019 67
Black phosphorus quantum dots/Ti ₃ C ₂ @TiO ₂	684.5		11.35 times		Solvent-heatmethod	Multilayer	300 W Xe lamp (λ > 420 nm)	Nanosheets	2020 68
									2020 69

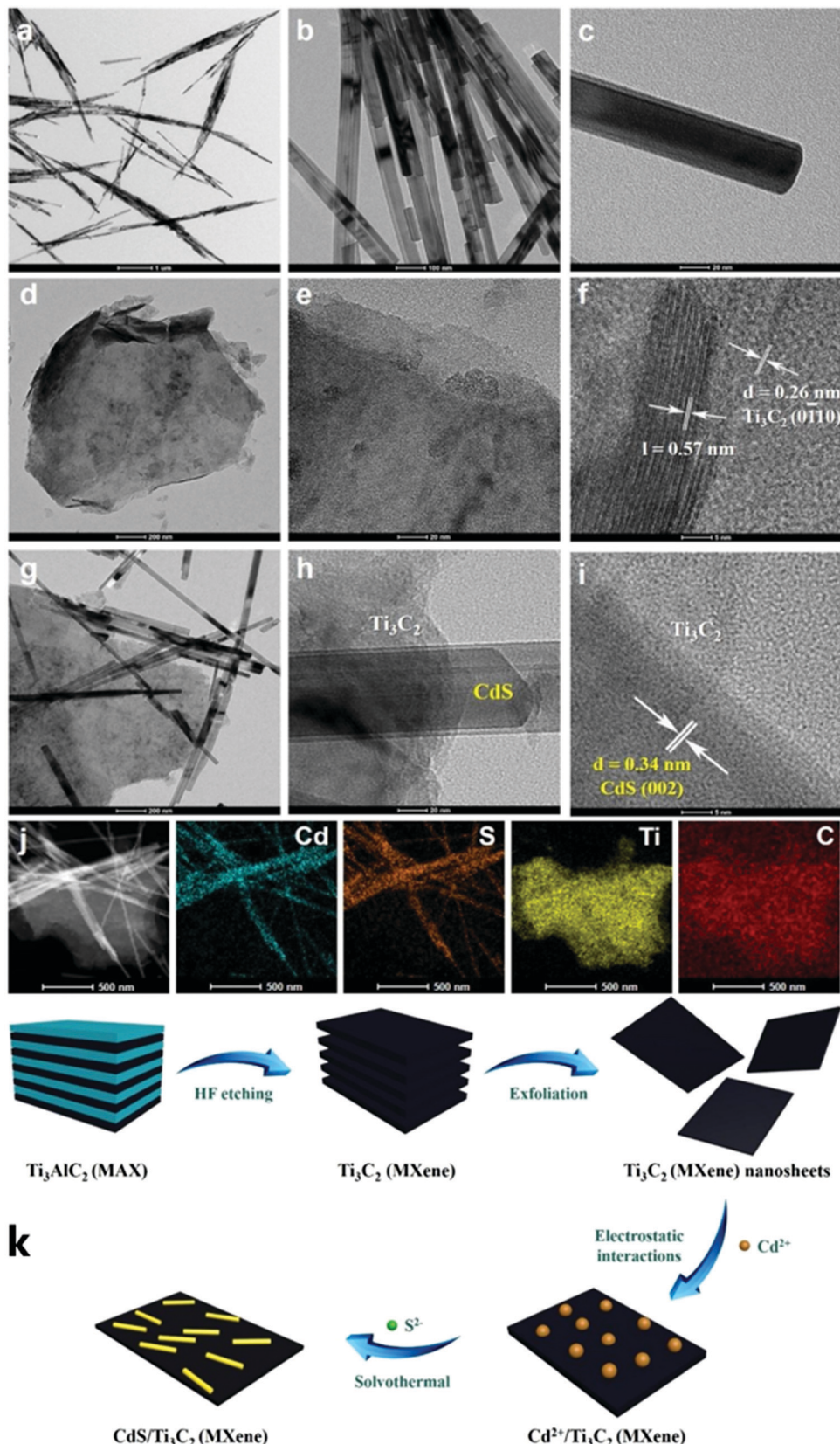


Fig. 5 TEM images of (a–c) CdS, (d–f) exfoliated Ti_3C_2 MXene nanosheets, (g–i) the composite CM-20, (j) the corresponding elemental mapping results of CM-20, and (k) the oxidation process of $\text{Ti}_3\text{C}_2\text{T}_x$.⁵²

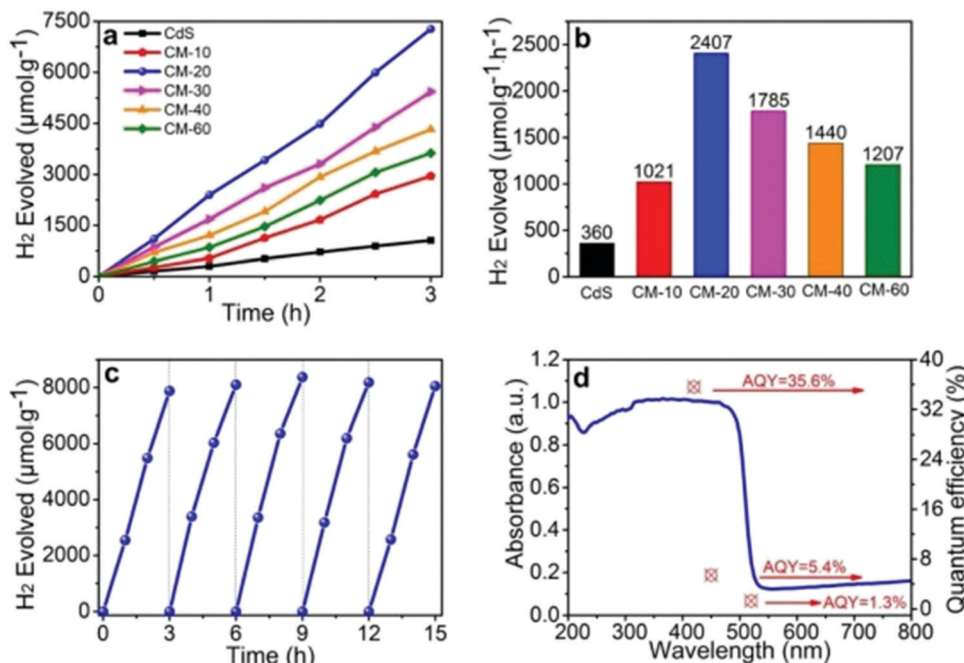


Fig. 6 (a and b) Photocatalytic H₂ evolution performance of different samples, (c) the recycled photocatalytic H₂ evolution experiments of CM-20, (d) AQY values and the wavelength dependence of photocatalytic H₂ evolution in the composite CM-20.⁵²

When Ti₃C₂T_x is oxidized, it is only the Ti atoms that are oxidized into the corresponding oxide (TiO₂), while the C atoms remain unchanged. In other words, MO comprises a sandwich structure of layered carbon layers and titanium oxide.³¹ Fig. 3 shows the structural evolution of Ti₃C₂T_x oxidation to MXene (MO). As can be seen from Fig. 3, MO maintains a layered structure, whilst the TiO₂ nanoparticles formed by oxidation are coated within the carbon layer structure. Due to the photoresponse capacity of TiO₂, this resulting structure is photocatalytically active. An example of this is MO/g-C₃N₄, which can photocatalytically split water with a relatively high efficiency.³²

The crystal structure of Ti₃C₂T_x contains Ti defects, which appear to contribute significantly to the instability of this material.^{14,33} High angle annular dark field (HAADF)-STEM imaging is an important tool in 2D materials' characterization and is used to unambiguously resolve the crystal structure and

defect configurations.^{34,35} As shown in Fig. 4, widespread Ti defects were directly detected through the HAADF-STEM imaging of the single-layer Ti₃C₂T_x flakes. Single-layered Ti₃C₂T_x obtained by HF etching was observed through HAADF-STEM images in Fig. 4(a)–(c). Fig. 4(d) was obtained by calculating tens of such images, and it reveals that the relationship between HF concentration and defect formation. It was found that vacancy clusters are rarely observed after etching with 2.7 wt% HF concentration but are relatively common after etching with 7 wt% HF.³³ Generally speaking, the average concentration of V_{Ti} (Ti vacancies) is positively related to that of HF.

3. Application in photocatalysis

Due to the excellent structural properties of Ti₃C₂T_x, there are many cases in which Ti₃C₂T_x is used as a co-catalyst in

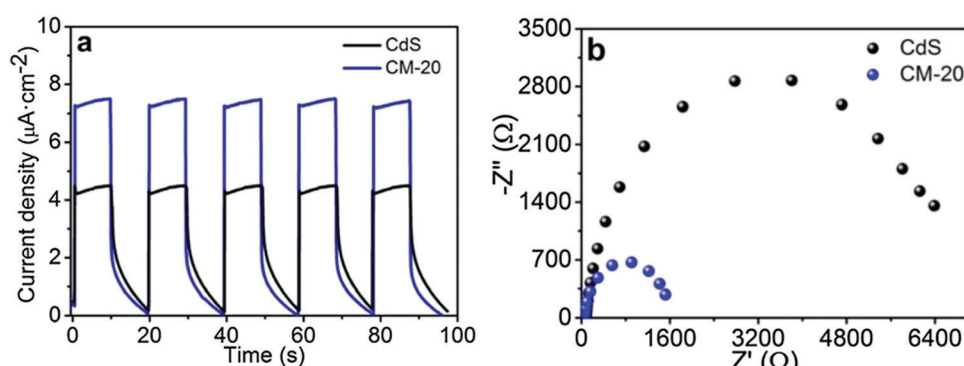


Fig. 7 (a) Photocurrent density curves and (b) EIS Nyquist plots of CdS and CM-20.⁵²



photocatalytic systems or is directly involved in photocatalytic reaction systems. This paper summarizes the application of $\text{Ti}_3\text{C}_2\text{T}_x$ in the field of photocatalysis from three aspects: photocatalytic hydrogen evolution reactions (HER), photocatalytic CO_2 reduction reactions (CO₂RR), and photocatalytic degradation reactions.

3.1 Application in HER

$\text{Ti}_3\text{C}_2\text{T}_x$ is the most widely used photocatalytic agent in hydrogen evolution reactions^{36–39} (HER). $\text{Ti}_3\text{C}_2\text{T}_x$ has the following advantages that make it ideal for use in photolysis: (a) hydrophilic surface functional groups are conducive for the adsorption of water molecules and promote the reaction; and (b) the Gibbs free energy of $\text{Ti}_3\text{C}_2\text{T}_x$ adsorption on hydrogen approaches zero infinitely, which is conducive for the reduction of H^+ .

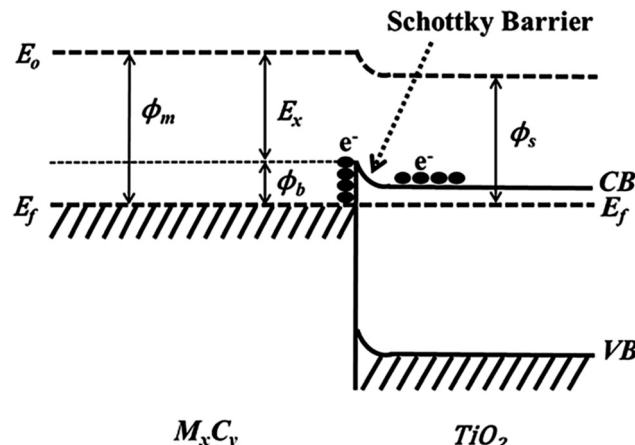
There are three important steps in the HER process, which are:^{30,40,41} (a) initial $\text{H}^+ + \text{e}^-$ formation; (b) generation of H^* (the intermediate adsorption state); and (c) formation of the $1/2 \text{ H}_2$ product. The adsorption state of H^* in process (b) directly affects the final hydrogen evolution efficiency and is an extremely important factor, which can be represented by the Gibbs adsorption free energy $|\Delta G_{\text{H}^*}|$. Through simulation calculations, it was found that when all the $\text{Ti}_3\text{C}_2\text{T}_x$ surface groups are $-\text{F}$, $\Delta G_{\text{H}^*} = -0.927 \text{ eV}$, and the adsorption is too strong. When all the surface groups are $-\text{O}$, $|\Delta G_{\text{H}^*}|$ is 0.003 eV, which is even better than the commonly used catalyst Pt ($\Delta G_{\text{H}^*} \approx -0.090 \text{ eV}$).^{42,43} Therefore, $\text{Ti}_3\text{C}_2\text{T}_x$ is a good HER co-catalyst. Examples of $\text{Ti}_3\text{C}_2\text{T}_x$ used for photolysis in recent years are summarized below (Table 1).

$\text{Ti}_3\text{C}_2\text{T}_x$ plays a significant role in HER, whether as a co-catalyst or as a part of the overall catalyst, as it greatly improves the performance of the base catalyst. As shown in Table 1, the presence of $\text{Ti}_3\text{C}_2\text{T}_x$ increases the yield of H_2 compared to solely the base catalyst by more than 2 times. The quantum efficiency is also significantly improved to 40.1%, whilst the maximum value of hydrogen production is 14.34 mmol $\text{g}^{-1} \text{ h}^{-1}$.

Monolayer $\text{Ti}_3\text{C}_2\text{T}_x$ or quantum dot $\text{Ti}_3\text{C}_2\text{T}_x$ displays better activity in HER. However, the use of monolayer $\text{Ti}_3\text{C}_2\text{T}_x$ as a photocatalyst has several disadvantages: (a) the preparation of monolayer $\text{Ti}_3\text{C}_2\text{T}_x$ is complex; (b) the structural stability is low and the catalyst is easily oxidized in water; (c) manipulation of the mono-layer or few-layer structures is not easy to carry out. Few-layer structures are presently prepared by electrostatic self-assembly or by *in situ* growth. The stability of the composite catalyst obtained by *in situ* growth is significantly greater than that obtained by electrostatic self-assembly.

Due to the surface hydrophilic groups,⁷⁰ suitable Gibbs adsorption free energies $|\Delta G_{\text{H}^*}|$, and excellent electron transfer efficiency, $\text{Ti}_3\text{C}_2\text{T}_x$ not only plays an important role in the three-step process of HER but can participate in electron hole separation.

Xiao *et al.* successfully synthesized the Schottky junction of 1D CdS nanorod/2D Ti_3C_2 MXene nanosheet in 2019.⁵² As shown in Fig. 5, Xiao *et al.* anchored Cd^{2+} using the deficiency of Ti on the Ti_3C_2 surface and the electrostatic interaction of free Cd^{2+} to prepare the 1D CdS nanorods. The composite material demonstrated excellent hydrogen production performance



Scheme 1 Formation of Schottky barrier at the MXene/TiO₂ interface.⁴⁵

($2407 \mu\text{mol h}^{-1} \text{ g}_{\text{catalyst}}^{-1}$), producing 6.68 times as much H_2 as pure CdS (Fig. 6).

Theoretically, the surface negative value (zeta potential value: $\sim 18 \text{ mV}$) of $\text{Ti}_3\text{C}_2\text{T}_x$ is sufficient to adsorb positively charged Cd^{2+} . $\text{Ti}_3\text{C}_2\text{T}_x$ treated with DMSO forms a low-layered structure, on which Cd^{2+} can be anchored and one-dimensional CdS nanorods can be grown. As shown in Fig. 5, due to the constraint effect of $\text{Ti}_3\text{C}_2\text{T}_x$, the length of 1D CdS nanorods in the 1D CdS nanorods/2D $\text{Ti}_3\text{C}_2\text{T}_x$ heterojunctions is smaller than that of the 1D CdS nanorods alone.

CdS equipped with $\text{Ti}_3\text{C}_2\text{T}_x$ displays excellent electrochemical properties. As shown in Fig. 7, the photocurrent of 1D CdS nanorods/2D $\text{Ti}_3\text{C}_2\text{T}_x$ was significantly better than that of one-dimensional CdS nanorods and the optical resistance was significantly lower than that of one-dimensional CdS nanorods. ESR tests show that the hydroxyl radical and superoxide radical signals of 1D CdS nanorods/2D $\text{Ti}_3\text{C}_2\text{T}_x$ were significantly enhanced after the addition of $\text{Ti}_3\text{C}_2\text{T}_x$. In conclusion, under the same illumination conditions, 1D CdS nanorods/2D $\text{Ti}_3\text{C}_2\text{T}_x$ generate more photogenic carriers. These produce oxygen-containing

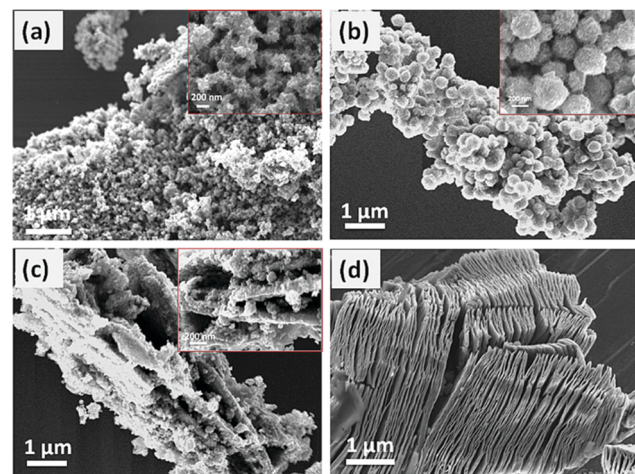


Fig. 8 SEM images of (a) TiO_2 (50 wt%), (d) $\text{Ti}_3\text{C}_2\text{T}_x$, (b) $\text{TiO}_2/\text{Ti}_3\text{C}_2\text{T}_x$ (5 wt%), and (c) $\text{TiO}_2/\text{Ti}_3\text{C}_2\text{T}_x$.⁴⁵



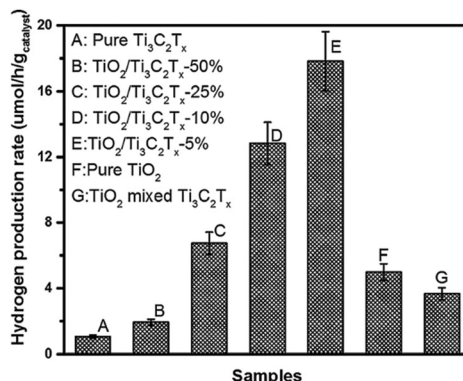


Fig. 9 (a) Photocatalytic hydrogen production rates and (b) recycling studies over the $\text{TiO}_2/\text{Ti}_3\text{C}_2\text{T}_x$ (5 wt%) sample.⁴⁵

groups with oxidizing reductivity, which can participate in photocatalytic hydrogenation reactions.

1D CdS nanorods/2D $\text{Ti}_3\text{C}_2\text{T}_x$ typically exhibit better visible light response, electron hole separation efficiency, and more effective carrier transport efficiency after the formation of multi-dimensional heterojunctions. This accounts for their excellent photocatalytic hydrogen evolution capability.

Using $\text{Ti}_3\text{C}_2\text{T}_x$ as the co-catalyst, Wang *et al.* synthesized a $\text{TiO}_2/\text{Ti}_3\text{C}_2\text{T}_x$ complex photocatalyst,⁴⁵ which was 4 times more efficient than pure phase TiO_2 in photohydrolyzing aquatic hydrogen. This is attributed to the Schottky barrier formed between TiO_2 and $\text{Ti}_3\text{C}_2\text{T}_x$, which effectively improves the separation efficiency of the electron holes. As shown in Scheme 1, excited electrons can be wired to $\text{Ti}_3\text{C}_2\text{T}_x$ from the conduction band of TiO_2 owing to the close contact between $\text{Ti}_3\text{C}_2\text{T}_x$ and TiO_2 ; thus, negative charge is accumulated in $\text{Ti}_3\text{C}_2\text{T}_x$ and a depletion layer formed at the metal–semiconductor interface, which is the Schottky barrier.⁴⁵

In this work, Wang *et al.* treated $\text{Ti}_3\text{C}_2\text{T}_x$ with DMSO to form low-layer structures. Amorphous TiO_2 was formed from TiCl_4 hydrolysis and then on the surface of $\text{Ti}_3\text{C}_2\text{T}_x$, amorphous TiO_2 was coated. After hydrothermal treatment, anatase $\text{TiO}_2/\text{Ti}_3\text{C}_2\text{T}_x$ material was formed, as shown in Fig. 8. Amorphous TiO_2 is micro-spherical and is coated on the surface of $\text{Ti}_3\text{C}_2\text{T}_x$, displaying

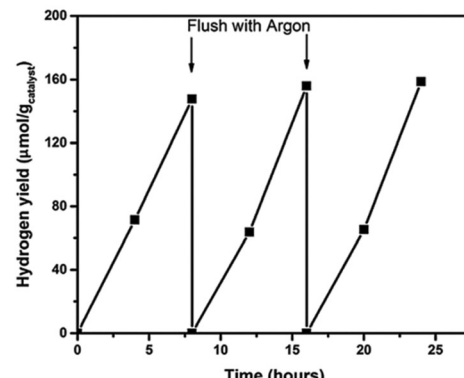


Fig. 9 (b) Recycling studies over the $\text{TiO}_2/\text{Ti}_3\text{C}_2\text{T}_x$ (5 wt%) sample.⁴⁵

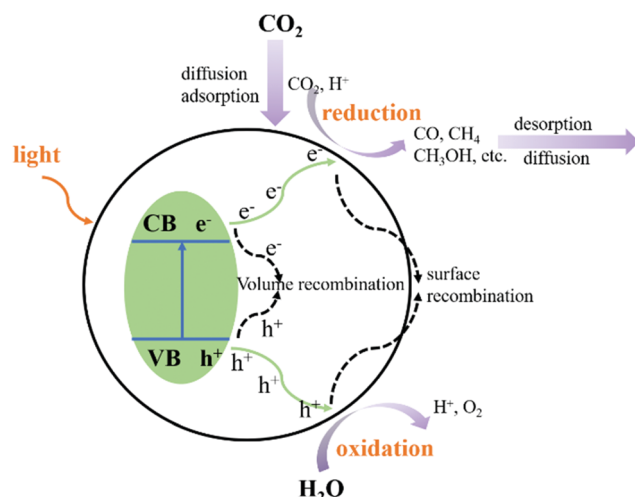


Fig. 11 CO_2RR process.

a low-layered structure (Fig. 8). After water heat treatment, the whole structure forms into a brittle cake structure (Fig. 9).

The $\text{TiO}_2/\text{Ti}_3\text{C}_2\text{T}_x$ material displays excellent photocatalytic hydrogen evolution capability with good cycling stability. The hydrogen production efficiency of $\text{TiO}_2/\text{Ti}_3\text{C}_2\text{T}_x$ -5% is about 4 times as high as

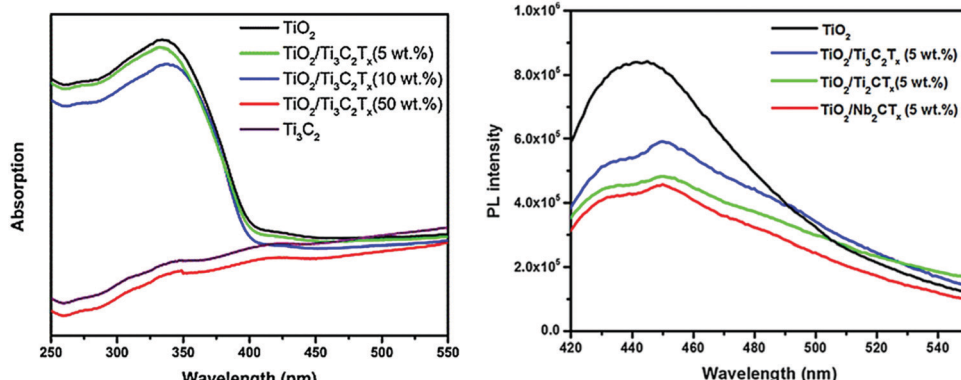


Fig. 10 (a) PL spectra and (b) DRS spectra of TiO_2 , $\text{TiO}_2/\text{Ti}_3\text{C}_2\text{T}_x$ (5 wt%), $\text{TiO}_2/\text{Ti}_3\text{C}_2\text{T}_x$ (10 wt%), and $\text{TiO}_2/\text{Ti}_3\text{C}_2\text{T}_x$ (50 wt%).⁴⁵

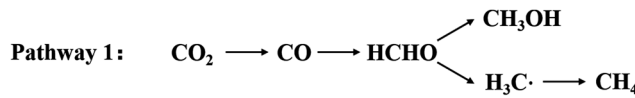


Fig. 12 Two pathways in CO_2RR .

that of pure phase TiO_2 , reaching $17.8 \mu\text{mol h}^{-1} \text{g}_{\text{catalyst}}^{-1}$. The hydrogen production efficiency of the 10% and 50% samples decreased slightly, which may be related to light energy absorption, as shown in Fig. 10(a). With the increase in $\text{Ti}_3\text{C}_2\text{T}_x$ addition, the light absorption capacity of the samples in the 250–380 nm region is gradually decreased. This significant improvement in the hydrogen production efficiency is closely related to the smooth carriage of $\text{Ti}_3\text{C}_2\text{T}_x$. As shown in Fig. 10(b), after the formation of the Schottky barrier, the carrier separation efficiency is improved, thus improving its photocatalytic capacity.

Thus, in conclusion, after loading with $\text{Ti}_3\text{C}_2\text{T}_x$, H_2 production increased at least twice. Such an amazing promotion is mainly related with 3 aspects of $\text{Ti}_3\text{C}_2\text{T}_x$: (a) it supplies a high throughput channel as a co-catalyst for the excited electrons while the holes cannot pass the boundaries; (b) its hydrophilicity; and (c) the Gibbs free energy of $\text{Ti}_3\text{C}_2\text{T}_x$ adsorption on hydrogen approaches zero infinitely.

3.2 Application in CO_2RR

The photocatalytic CO_2 reduction reaction (CO_2RR) consists of five steps:^{71–74} light absorption, charge separation, CO_2 adsorption, surface redox reaction, and product desorption. As shown in Fig. 11, when the CB of the photocatalyst is greater than the redox potential of CO_2 , and charge separation occurs whilst the electrons and holes recombine. Several complex factors dictate which of these two competing processes predominantly occurs. After the adsorption of CO_2 and the migration of photogenerated electrons and holes from the inside of the crystal structure to the

surface, the redox reaction is carried out on the surface of the catalyst. The product then de-attaches, which completes the entire photocatalytic CO_2 reduction reaction.

$\text{Ti}_3\text{C}_2\text{T}_x$ is also widely used in the photocatalytic CO_2 reduction reaction. However, due to its own carbon source and instability, further research is needed to understand the mechanism of photocatalytic CO_2 reduction of $\text{Ti}_3\text{C}_2\text{T}_x$.

In 2017, Zhang *et al.* summarized the CO_2 reduction capacity of three MXene materials with surface groups, which terminate with $-\text{O}$ through theoretical calculations.⁷⁵ Among the three materials, Ti_2CO_2 , V_2CO_2 , and $\text{Ti}_3\text{C}_2\text{O}_2$, Ti_2CO_2 showed the best photocatalytic CO_2 reduction capacity. Of the two reduction paths^{76–78} shown in Fig. 12, the pathway of “ $\text{CO}_2\text{--HCOO--HCOOH}$ ” has a favorable energy barrier of about 0.53 eV.

Through DFT calculations, it was revealed that in the first step reaction of CO_2 adsorption in CO_2RR , the O atom of the CO_2 molecule occupies an O defect position on the MXene. This mode in adsorption requires the lowest energy. The adsorption energies of the three materials were $\text{Ti}_3\text{C}_2\text{O}_2$ (−0.73 eV), Ti_2CO_2 (−0.67 eV), and V_2CO_2 (−0.35 eV). Ti_2CO_2 has a lower adsorption energy compared to V_2CO_2 as the Ti atoms are more likely to lose electrons than the V atoms.

If the reaction proceeds *via* pathway 1 (Fig. 11), one of the oxygen atoms of the CO_2 molecule is captured by the oxygen defect. This results in the breaking of the C–O bond, while CO is produced. In this step, $\text{Ti}_3\text{C}_2\text{O}_2$ would lower the energy barrier of the C–O bond to about 0.86 eV. Pathway 2 (Fig. 11) has an energy barrier greater than 1 eV. In this pathway, the CO_2 molecules are captured by an oxygen defect on the surface of MXene and are hydrogenated to form COOH. This is further hydrogenated and converted into the products CO and H_2O . CO, which is produced, can further react to form HCOOH, HCOH, CH_2OH , CH_4 , and other products.

Studies into the application of $\text{Ti}_3\text{C}_2\text{T}_x$ in CO_2RR is summarized in Table 2.

In 2018, Cao *et al.* prepared a 2D/2D heterogeneous junction of $\text{Ti}_3\text{C}_2\text{T}_x/\text{Bi}_2\text{WO}_6$ and the composite showed excellent photocatalytic CO_2 reduction performance.⁸² As shown in Fig. 13,

Table 2 Comparison of photocatalysts including $\text{Ti}_3\text{C}_2\text{T}_x$ in CO_2RR

Photocatalyst	Products and yield ($\mu\text{mol g}^{-1} \text{h}^{-1}$)	Activity improvement factor	Reaction conditions	Light source	Preparation method	Morphology	Monolayer or Multilayer	Year	Ref.
2D/2D $\text{Ti}_3\text{C}_2\text{MXene/g-C}_3\text{N}_4$ nanosheet	CO (5.19) CH ₄ (0.044)	8.37 (CO) 2.09 (CH ₄)	20 mg catalyst gas-solid	300 W Xe lamp ($\lambda > 420 \text{ nm}$)	Calcination under N ₂ atmosphere	2D/2D nanosheets	Monolayer	2020	79
Alklinized $\text{Ti}_3\text{C}_2\text{/g-C}_3\text{N}_4$ decorating $\text{g-C}_3\text{N}_4$	CO (11.21 $\mu\text{mol g}^{-1}$) CH ₄ (0.044 $\mu\text{mol g}^{-1}$)	5.96 (CO) 5.6 (CH ₄)	40 mg catalyst gas-solid	300 W Xe lamp ($\lambda > 420 \text{ nm}$)	Alkali etching	3D	Multilayer	2019	80
$\text{TiO}_2/\text{Ti}_3\text{C}_2$	CO CH ₄ (0.22)	—	50 mg catalyst liquid-solid	300 W Xe lamp	Calcination	Nanoparticles	Multilayer	2018	81
2D/2D ultrathin $\text{Ti}_3\text{C}_2/\text{Bi}_2\text{WO}_6$	CO CH ₄ (1.78)	4.34 (CH ₄) 6.28 (CH ₃ OH)	100 mg catalyst liquid-solid	Xe lamp	Hydrothermal	Flat shape structure	2D Monolayer	2018	82
2D/2D/0D $\text{TiO}_2/\text{C}_3\text{N}_4/\text{Ti}_3\text{C}_2$	CH ₃ OH (0.44) CO (4.39) CH ₄ (1.20)	1.39 (CO) (than $\text{TiO}_2/\text{C}_3\text{N}_4$)	30 mg catalyst liquid-solid	300 W Xe lamp	Electrostatic self-assembly	2D/2D structure	Ti ₃ C ₂ quantum dots	2020	83



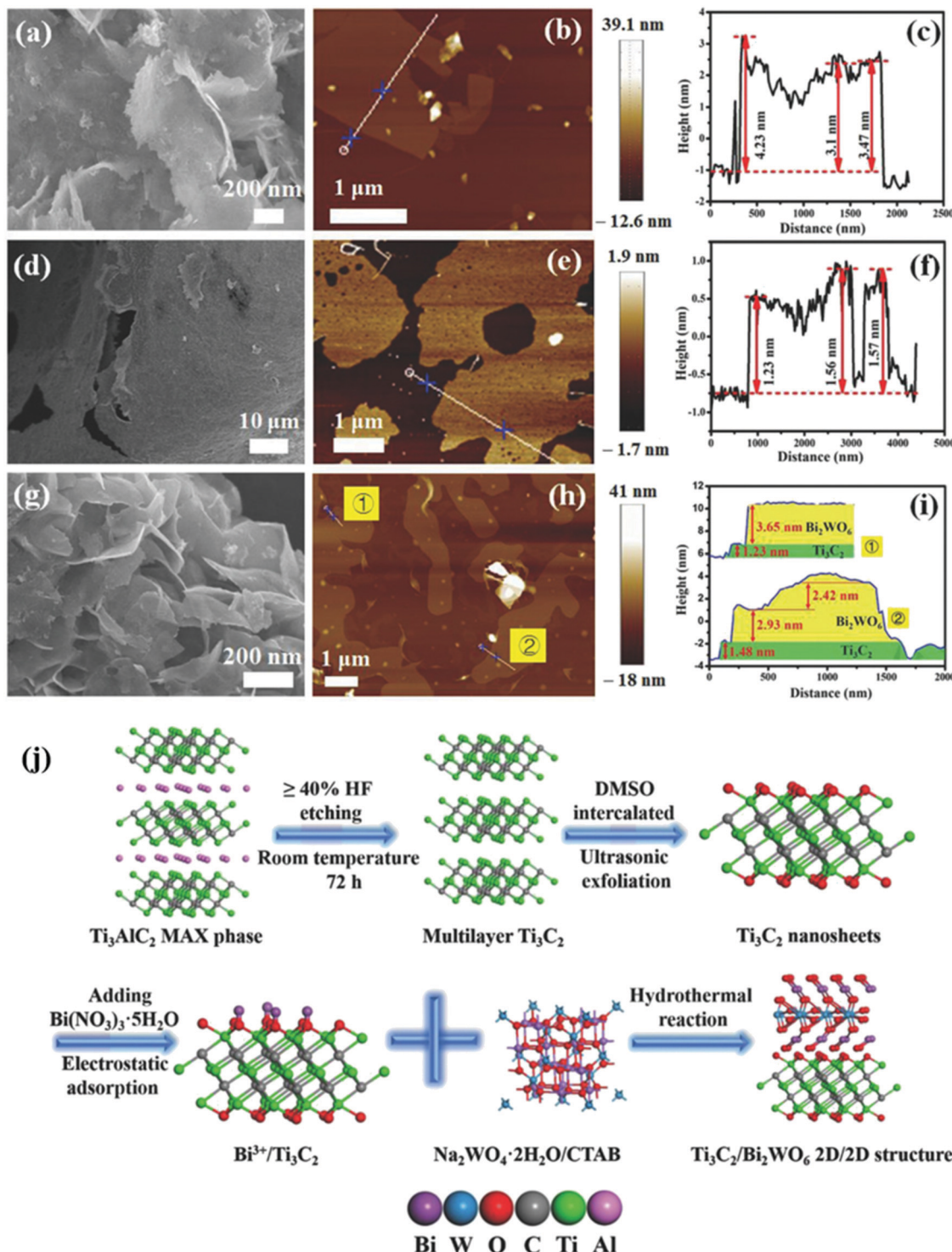


Fig. 13 (a–c) Typical FESEM, AFM images, and height cutaway view of Bi_2WO_6 , (d–f) Ti_3C_2 nanosheets, (g–i) TB2 ($\text{Ti}_3\text{C}_2\text{T}_x/\text{Bi}_2\text{WO}_6$), and (j) schematic illustration of the synthetic process.⁸²

multi-layer structure $\text{Ti}_3\text{C}_2\text{T}_x$ was tested with DMSO. After the formation of low-layer structure $\text{Ti}_3\text{C}_2\text{T}_x$, the oxygen-rich surface was negatively charged, which permitted Bi^{3+} to be adsorbed from hydrolyzed $\text{Bi}(\text{NO}_3)_3 \cdot 5\text{H}_2\text{O}$.⁸⁴ After the addition of a tungsten source, a 2D/2D $\text{Ti}_3\text{C}_2\text{T}_x/\text{Bi}_2\text{WO}_6$ heterojunction was

formed. The concurrent addition of CTAB furthermore ensures the ultrathin structure of both Bi_2WO_6 ⁸⁵ and $\text{Ti}_3\text{C}_2\text{T}_x$.⁸⁶

The successful preparation of heterojunctions greatly enhances the ability of Bi_2WO_6 to reduce CO_2 . The CH_4 production of the sample TB2 reached $1.78 \mu\text{mol h}^{-1} \text{g}^{-1}$, while

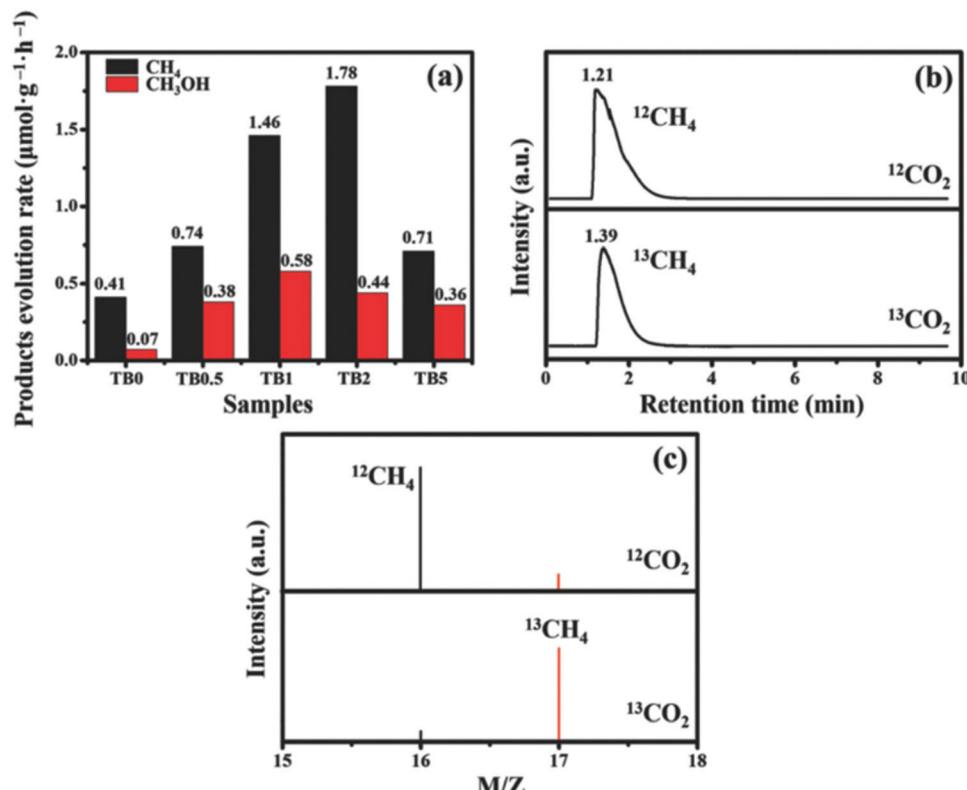


Fig. 14 (a) Photocatalytic activity of TB0 to TB5; (b) GC-MS spectra over TB2 after irradiation for several hours with different carbon sources; (c) GC-MS analysis of the reaction products with ¹²C and ¹³C as carbon sources.⁸²

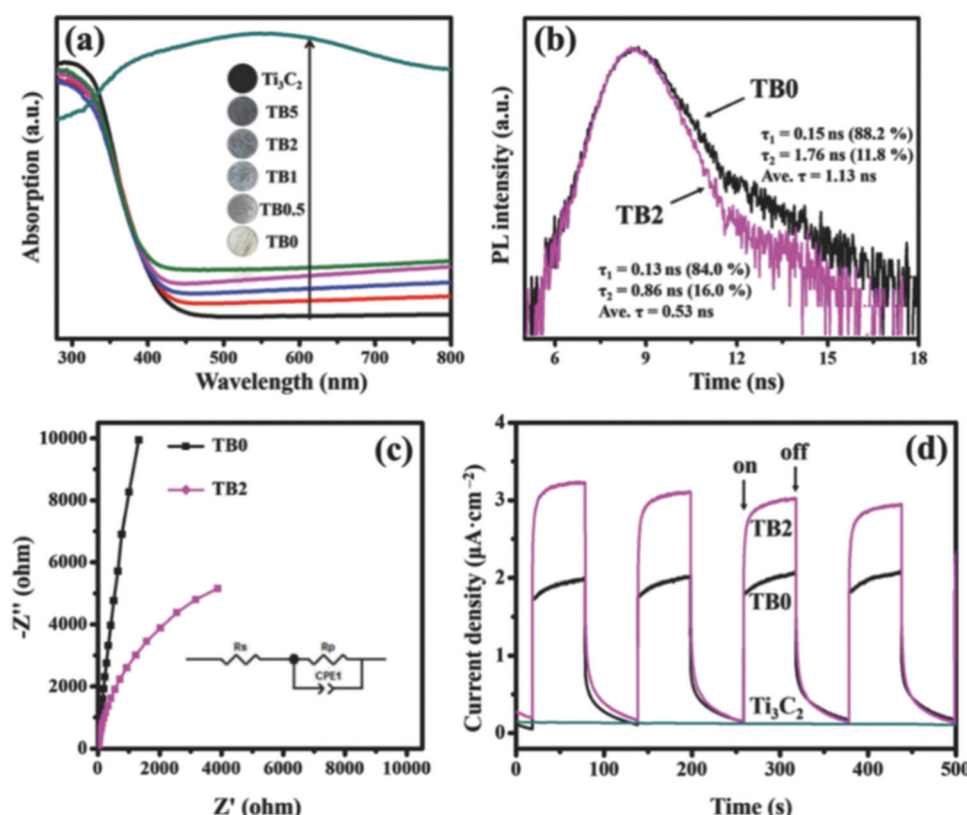


Fig. 15 (a) UV-Vis DRS of all the as-prepared samples; (b) TRPL spectra of TB0 and TB2; (c) EIS plots and (d) transient photocurrent of the prepared samples.⁸²

the yield of CH_3OH reached $0.44 \mu\text{mol h}^{-1} \text{ g}^{-1}$. The isotopic spectra of Fig. 14(b) and (c) indicates that the produced CH_4 and CH_3OH are formed from the photocatalytic reduction of CO_2 .

As shown in Fig. 15(a), $\text{Ti}_3\text{C}_2\text{T}_x$ exhibits excellent light absorption performance between 200–800 nm. The light absorption capacity of Bi_2WO_6 was also significantly improved by carrying $\text{Ti}_3\text{C}_2\text{T}_x$. To be noted, as shown in Fig. 14(b), the fluorescence lifetime decreased after loading with $\text{Ti}_3\text{C}_2\text{T}_x$. This is because TC supplies a more efficient non-radiative decay pathway. In electrochemical tests, the photocurrent photoelectric impedance spectrum further revealed that the carriage of $\text{Ti}_3\text{C}_2\text{T}_x$ greatly promoted the carrier strength of Bi_2WO_6 . This further confirmed the successful construction of the $\text{Ti}_3\text{C}_2\text{T}_x/\text{Bi}_2\text{WO}_6$ heterojunction.

Yang *et al.* prepared 2D/2D Ti_3C_2 MXene/g-C₃N₄ heterojunctions in 2020.⁷⁹ As shown in Fig. 16(g), Ti_3AlC_2 was successfully etched to form Ti_3C_2 , as indicated by the XRD patterns.^{87,88} 2D g-C₃N₄ was found to grow on the surface of Ti_3C_2 under an atmosphere of N_2 . The formed 2D/2D Ti_3C_2 MXene/g-C₃N₄ demonstrated excellent photocatalytic CO_2 reduction capability. As shown in Fig. 17, the photocatalytic performance of pure phase g-C₃N₄ for the production of CO and CH_4 is only $0.62 \mu\text{mol h}^{-1} \text{ g}^{-1}$ and $0.021 \mu\text{mol h}^{-1} \text{ g}^{-1}$, respectively, in contrast to Ti_3C_2 , wherein the production of CO and CH_4 is $5.19 \mu\text{mol h}^{-1} \text{ g}^{-1}$, $0.44 \mu\text{mol h}^{-1} \text{ g}^{-1}$, respectively. The isotopic experiments confirm that the product is produced by the photocatalytic reduction of CO_2 .

The tests of PL and TRPL showed that the composite rate of electron holes^{45,89} decreased significantly after carrying Ti_3C_2 . As shown in Fig. 18(b), the fitted pure phase C₃N₄ had a lifetime of only 4.14 ns, while 10TC had a lifetime of 4.51 ns, which represents a significant increase in the lifetime of the carriers. This is closely related to the smooth carrying of Ti_3C_2 . An excellent “storage capacitor” is produced when Ti_3C_2 forms a heterojunction with g-C₃N₄. When the electrons are transmitted to the semiconductor surface, they transfer to Ti_3C_2 quickly while the holes cannot. This greatly reduces the electron hole composite and improves the photocatalytic performance of the material. On the other hand, abundant defects on the Ti_3C_2 surface provide excellent sites for CO_2 adsorption.

In conclusion, the application of $\text{Ti}_3\text{C}_2\text{T}_x$ in CO_2RR is relatively less than that of photocatalytic water splitting. This is because of its instability and its own carbon resources, which can cause interferences during the photocatalytic CO_2 reduction reaction. As shown in Table 2, among limited reports, $\text{Ti}_3\text{C}_2\text{T}_x$ with both single-layered structures and multi-layered structures shows an obvious production promotion. It is to be noted that there are no new products (such as C₂ products, formaldehyde, and methyl ether) after loading with $\text{Ti}_3\text{C}_2\text{T}_x$ compared to the base photocatalyst. This phenomenon confirms that $\text{Ti}_3\text{C}_2\text{T}_x$ cannot change the energy barrier of the base photocatalyst for CO_2 reduction. Thus, in general, the obvious promotion during CO_2RR may be related to the two features of $\text{Ti}_3\text{C}_2\text{T}_x$: (a) abundant surface vacancies for CO_2 adsorption and (b) promoting the separation of carriers.

3.3 Applications in degradation

The main principle of photocatalytic degradation by photocatalytic semiconductor materials is that light stimulates the generation of oxidizing holes.^{90–93} These can oxidize dissolved oxygen into efficient oxygen-active species such as superoxide radicals (O_2^-), singlet oxygen (O), and hydroxyl radicals (OH). These species can directly oxidize the substrate.^{94–96} Ti_3C_2 has a wealth of surface groups and active sites, which are conducive for the adsorption of substrates. Accordingly, Ti_3C_2 has been of particular interest as a photoactive degradation catalyst. A summary of the previous studies investigating the application of Ti_3C_2 in photocatalytic degradation reactions is shown in Table 3.

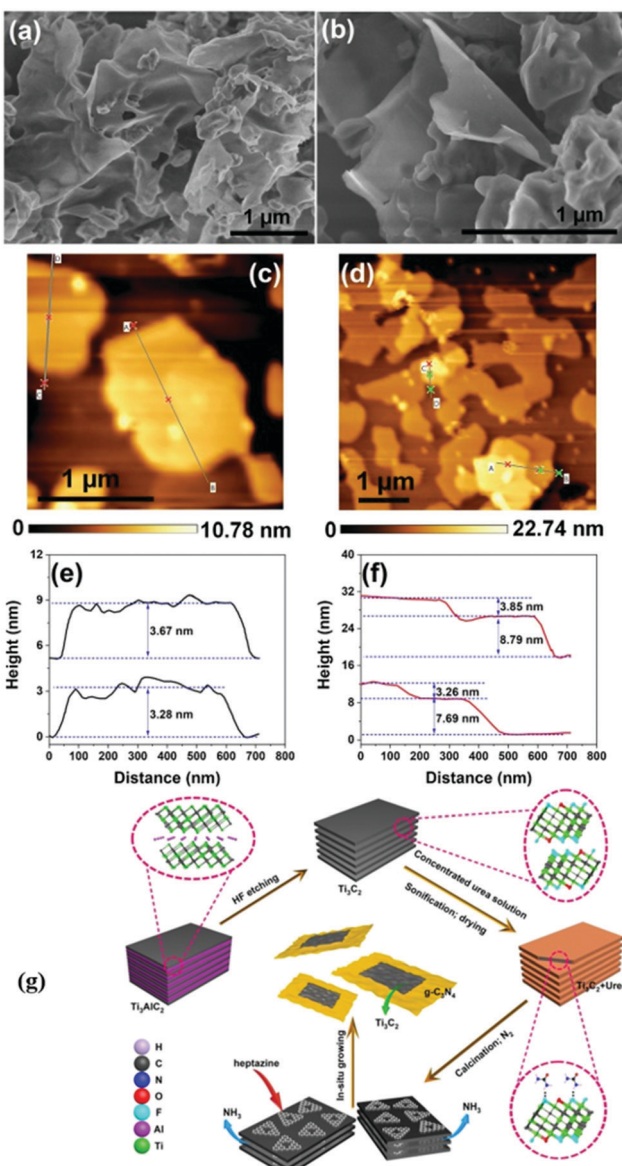


Fig. 16 FESEM images of UCN (a) and 10TC (b) samples, AFM images and the corresponding height profiles of UCN (c and e), 10TC (d and f) samples, and (g) schematic illustration for the fabrication process.⁷⁹



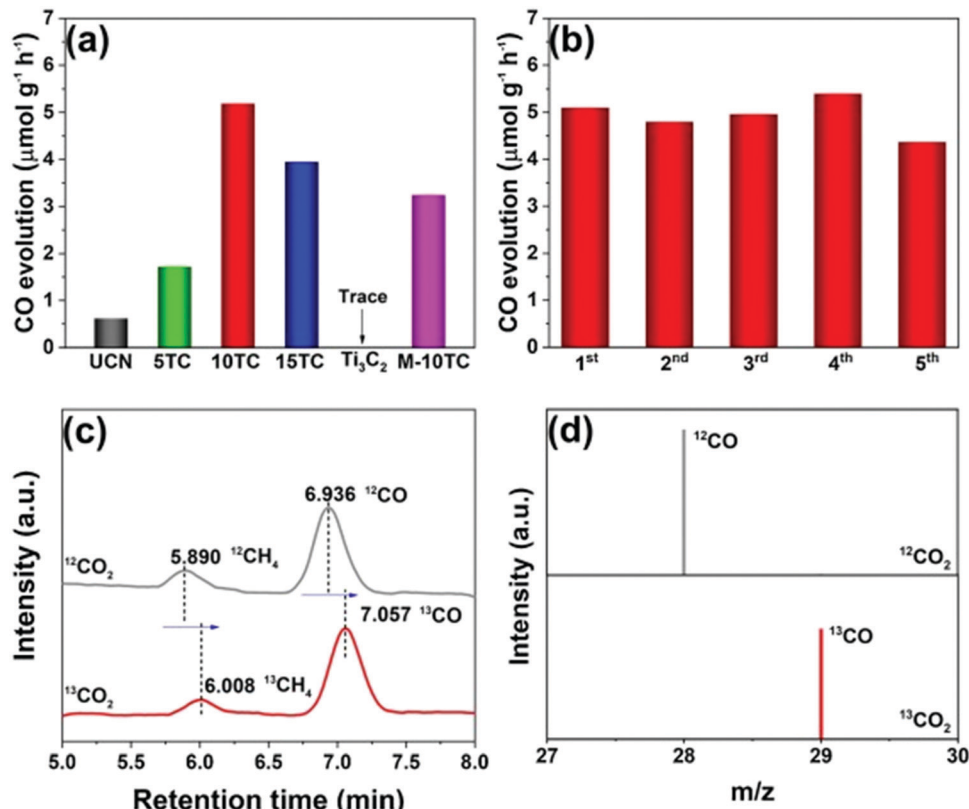


Fig. 17 Photocatalytic CO₂ reduction performance of the as-prepared samples (a); cycling tests over the 10TC sample (b); GC-MS analysis of the products from the photoreduction of CO₂ over 10TC using labelled ¹²CO₂ and ¹³CO₂ as the carbon sources (c and d).⁷⁹

In 2018, Cai *et al.* produced a Ag₃PO₄/Ti₃C₂ composite photocatalyst, which possessed excellent photocatalytic degradation performance.⁸⁷

As shown in Fig. 19, after DMSO and sonication treatment, Ti₃C₂ with a low-layer structure was formed. After the addition of silver nitrate, Ag⁺ was adsorbed due to the negative charge on the surface of Ti₃C₂. Ag₃PO₄ nanoparticles were grown *in situ*, forming a heterojunction between the Ag₃PO₄ nanoparticles and the Ti₃C₂ nanosheets.

As shown in Fig. 20, the heterojunction of the Ag₃PO₄ nanoparticles/Ti₃C₂ nanosheets shows a photocatalytic degradation stage rate K of 0.094, 0.005, 0.32, and 0.0042 min⁻¹ for methyl orange (MO), 2,4-dinitrophenol (2,4-DNP), tetracycline (TC-H), thiampenicol (TPL), and chloramphenicol (CPL), respectively. According to EPR analysis, the hydroxyl radical (•OH) plays an important role in the oxidation system, as shown in Fig. 20(f). This may be related to abundant Ti defects on the Ti₃C₂ surface. Ti sites exposed on the surface of Ti₃C₂ have strong redox reactivity, which promotes multiple electron reduction reactions (O₂ → H₂O₂ → •OH).

As shown in Fig. 21, PL, TRPL, and the electrochemical characterization spectra indicate that the carrier separation efficiency of the material is significantly improved after carrying Ti₃C₂. This may be attributed to (i) the abundant surface hydrophilic functional groups of the Ti₃C₂ construct, which have strong interfacial contact with Ag₃PO₄, facilitating the separation

of carriers; (ii) the strong redox reactivity of the surface Ti sites, which promote multiple electron reduction reactions to induce more •OH production; and (iii) a Schottky junction formed at the Ag₃PO₄/Ti₃C₂ interface enabling efficient transfer electrons to the Ti₃C₂ surface. This inhibits the photocossion of Ag₃PO₄ caused by photogeneration electrons.

Under high temperature conditions, Ti in the Ti₃C₂ skeleton layer is oxidized into TiO₂, while C still exists in the form of a graphene-like layer. Therefore, under high temperature conditions, Ti₃C₂ can be converted into amorphous TiO₂ anchored within the graphene-like layer. In 2020, Wu *et al.* took advantage of this material, which displayed excellent photocatalytic degradation performance.¹⁰⁵

As shown in Fig. 22(e) and (f), high temperature treated Ti₃C₂ still retains its morphology and a 3D block-shaped morphology is formed after carrying g-C₃N₄ (Fig. 23).

Graphene layers anchored to TiO₂/g-C₃N₄ show first-order kinetic constants for the degradation of rhodamine B (RhB), tetracycline (TC), ciprofloxacin (CIP), and bisphenol A (BPA) of 0.0559, 0.0244, 0.0168, and 0.0194 min⁻¹, respectively. According to the EPR test results (Fig. 24(a)–(d)), the oxygen active species that play a role in the oxidation process mainly include •O₂⁻ and •OH. Furthermore, signals corresponding to the holes (h⁺) were also detected. The contribution to the degradation of these test molecules appears to be in the order of •O₂⁻ > h⁺ > •OH.

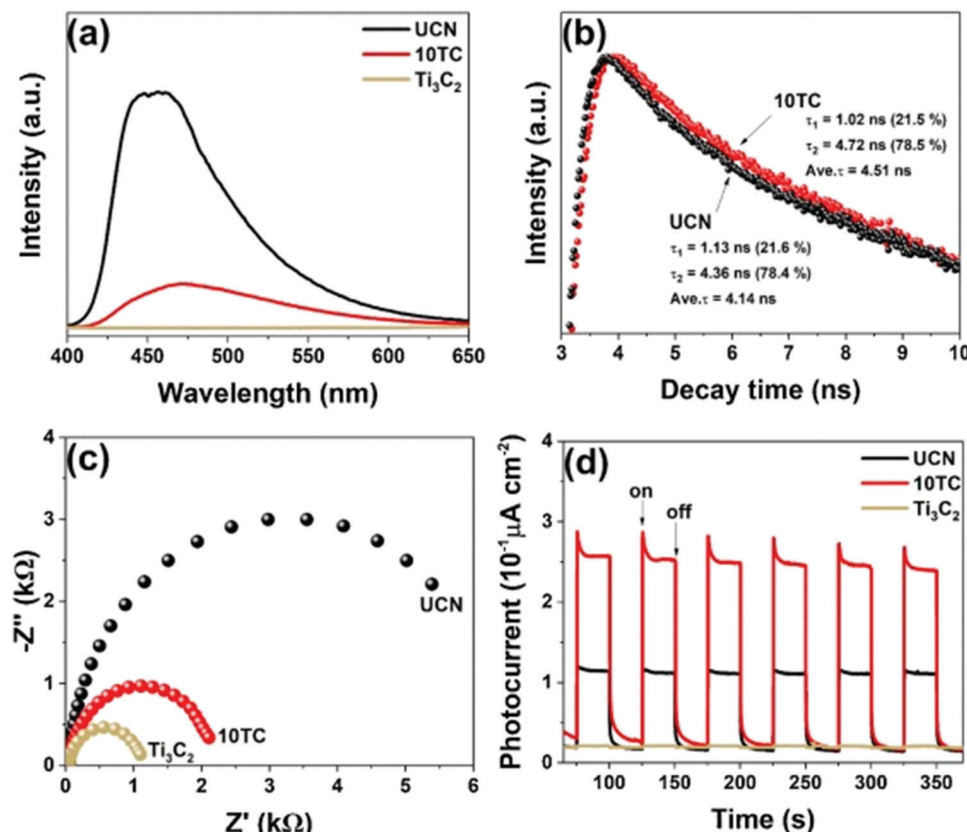


Fig. 18 PL spectra, EIS, and TPR plots of UCN, Ti_3C_2 , and 10TC samples (a, c, and d); TR-PL spectra of UCN and 10TC (b).⁷⁹

High-temperature treated Ti_3C_2 has a greatly enhanced light absorption capacity, whilst the carrier separation efficiency and transmission efficiency are also improved. The improvement of the photocurrent (Fig. 24(e) and (f)) also verified that the graphene layers anchoring TiO_2 lead to the formation of a heterogeneous junction. This is due to the change in the electric field between $\text{g-C}_3\text{N}_4$.

In conclusion, as a co-catalyst, the application of $\text{Ti}_3\text{C}_2\text{T}_x$ in photocatalytic degradation is mainly due to its three characteristics: (a) in a liquid–solid phase reaction, its hydrophilicity makes it easy for the adsorption or contact between the pollutants and photocatalysts; (b) high throughput electron transfer makes it easier to generate concentrated holes (h^+); and (c) Ti sites exposed on the surface of Ti_3C_2 have strong redox reactivity, which promotes multiple electron reduction reactions, such as the reaction of activating molecular oxygen ($\text{O}_2 \rightarrow \text{H}_2\text{O}_2 \rightarrow \cdot\text{OH}$).

4. Challenges

The application of $\text{Ti}_3\text{C}_2\text{T}_x$ in photocatalysis is worthy of further investigation, despite the many problems that need to be solved. The main issue lies in the instability of the composite material, resulting in unstable photocatalytic performance. This contributes to the difficulty in determining the photocatalytic process mechanisms of $\text{Ti}_3\text{C}_2\text{T}_x$ -based photocatalysts. Many of the existing solutions use either few- or single-layer structured materials. However, the preparation process of these

is complex. Despite this, $\text{Ti}_3\text{C}_2\text{T}_x$ has an excellent optical response ability and displays broad catalytic activity.

5. Summary and outlook

5.1 Summary

In recent years, $\text{Ti}_3\text{C}_2\text{T}_x$ has attracted wide interest as a photocatalytic material due to its rich surface space and surface defects, hydrophilic properties, large interlayer spacing, and excellent microwave absorbing properties. $\text{Ti}_3\text{C}_2\text{T}_x$ -based photocatalysts are widely used in hydrogen evolution reactions (HER), CO_2 reduction reactions (CO₂RR), photocatalytic degradation reactions, and show excellent catalytic performance. The application of $\text{Ti}_3\text{C}_2\text{T}_x$ in photocatalysis still warrants further investigation.

The further application of $\text{Ti}_3\text{C}_2\text{T}_x$ in photocatalysis depends on the development of the material itself. Methods to improve the stability of the $\text{Ti}_3\text{C}_2\text{T}_x$ structure need to be explored, starting from synthetic methods. In addition, the rich groups on the surface of $\text{Ti}_3\text{C}_2\text{T}_x$ and its hydrophilicity should be further explored, particularly in photocatalytic liquid phase reactions.

5.2 Outlook

5.2.1 Mechanism. During the photocatalytic reaction, especially the reaction including liquid phase, the mechanism

Table 3 Application of $\text{Ti}_3\text{C}_2\text{T}_x$ in photocatalytic degradation reactions

Photocatalyst	Substrate of degradation	Removal rate (%)/rate constants (min ⁻¹)	Reaction conditions	Light source	Oxygenic species	Morphology	Monolayer or multilayer	Year	Ref.	
$\text{Ag}_3\text{PO}_4/\text{Ti}_3\text{C}_2$	Methyl orange (MO)	(rate constants) 0.094 (MO)	20 mg catalyst + 50 mL 20 mg L ⁻¹ substrate, 30 min dark adsorption	300 W Xe lamp ($\lambda > 420$ nm)	h^+ (main)	2D $\text{Ti}_3\text{C}_2/\text{Ag}_3\text{PO}_4$ particles	Monolayer	2018	87	
2,4-Dinitrophenol (2,4-DNP) Tetracycline hydrochloride (TC-H)	2,4-DNP (0.005) TC-H (0.32)			•OH						
Thiamphenicol (TPL) Chloramphenicol (CPL) UO_2^{2+}	TPL (0.0042) CPL (0.025) (Removal rate)	20 mg catalyst + 60 mL 50 ppm substrate, 8 hours dark adsorption	300 W Xe lamp ($\lambda = 320$ –2500 nm)	•OH	2D $\text{Ti}_3\text{C}_2/\text{SrTiO}_3$ particles	Multilayer	2019	97		
$\text{Ti}_3\text{C}_2\text{-OH/Bi}_2\text{WO}_6$ composites	Rhodamine B	(Rate constants) 0.0596	77% in 180 min 10 mg catalyst + 50 mL 2 \times 10 ⁻⁵ mol L ⁻¹ substrate, 30 min dark adsorption	300 W Xe lamp ($\lambda = 400$ –2500 nm)	h^+	Porous spherical structure	$\text{Ti}_3\text{C}_2\text{-OH}$	2019	98	
$\text{MoS}_2@\text{Ti}_3\text{C}_2$ Nanohybrid	Liquid paraffin (LP)	(Rate constants) 0.0476	A certain amount of sample + 2.0 g of deionized water and 1.0 g of LP + 10 mL dichloromethane as the sacrifice reagent, 30 min dark adsorption	1000 W high-pressure mercury lamp		MoS_2 nanosheets/ Ti_3C_2 sheets	Multilayer	2019	99	
0D/2D $\text{Bi}_3\text{TaO}_7/\text{Ti}_3\text{C}_2$	Methylene blue	(Rate constants) 0.032	50 mg catalyst + 100 mL 300 W Xe lamp ml 10 mg L ⁻¹ ($\lambda > 420$ nm)	•OH	Bi_3TaO_7 nanoparticles/ Ti_3C_2 nanosheets	Multilayer	2020	100		
2D/2D $\text{Ti}_3\text{C}_2/\text{Porous g-C}_3\text{N}_4$	Phenol	(Rate constants) 0.022	Substrate, 60 min dark adsorption 20 mg catalyst + 50 mL 10 mg L ⁻¹ ($\lambda > 400$ nm)	500 W Xe lamp	2D/2D $\text{Ti}_3\text{C}_2/\text{PCN}$ nanocomposite	Multilayer with ultrasonication	2020	101		
$\text{CdS}@\text{Ti}_3\text{C}_2@\text{TiO}_2$	Sulfachloropyridazine (SCP)	(Removal rate) (about 95% in 60 min)	Substrate, 30 min dark adsorption 50 mg catalyst + 200 mL 20 mg L ⁻¹ ($\lambda = 400$ –1050 nm)	•O ₂ ⁻ 300 mW cm ⁻² ($\lambda = 400$ –1050 nm)	CdS nanoparticles/ $\text{Ti}_3\text{C}_2@\text{TiO}_2$ bulk	Multilayer	2019	102		
Methylene blue (MB)	MB (about 80% in 60 min)									
Rhodamine B (RhB)	RhB (about 99% in substrate, 30 min in 60 min)									
Phenol	Phenol (about 50% in 60 min)									
(111) $\text{TiO}_{2-x}/\text{Ti}_3\text{C}_2$	Mmethylene blue (MB)	(Removal rate) MB (75% in 150 min)	10 mg catalyst + 200 mL 20 mg L ⁻¹ ($\lambda > 400$ nm)	h^+ (main)	TiO_2 nanoparticles/ Ti_3C_2 nanosheets	Multilayer	2017	103		
(001) $\text{TiO}_2/\text{Ti}_3\text{C}_2$	Methyl orange (MO)	(Rate constants) 0.018	10 mg catalyst + 200 mL 20 mg L ⁻¹ substrate, 60 min dark adsorption	300 W Xe lamp	h^+ (main)	TiO_2 square nanosheets/ Ti_3C_2 nanosheets	Multilayer	2016	104	

Table 3 (continued)

Photocatalyst	Substrate of degradation	Removal rate (%)/rate constants (min ⁻¹)	Reaction conditions	Light source	Oxygenic species	Morphology	Monolayer or multilayer	Year	Ref.
Graphene layers anchored TiO ₂ /g-C ₃ N ₄	Rhodamine B (RhB)	(Rate constants) 0.0559 (RhB)	10 mg catalyst + 200 mL (RhB) 20 mg L ⁻¹ , TC 10 mg L ⁻¹ , CIP 3 mg L ⁻¹ , BPA 5 mg L ⁻¹ , 60 min dark adsorption	300 W Xe lamp (λ > 400 nm)	•OH	3D bulk	Bulk Ti ₃ C ₂ @TiO ₂	2020	105
2D/2D Ti ₃ C ₂ /MoS ₂	Tetracycline (TC) Ciprofloxacin (CIP) Bisphenol A (BPA) Methylene orange (MO)	0.0244 (TC) 0.0168 (CIP) 0.0194 (BPA) (Rate constants) 0.00836	50 mg catalyst + 50 mL 20, 30, 50 mg L ⁻¹ substrate, 30 min dark adsorption, 60 min dark adsorption	400 W metal halide lamp	•O ₂ ⁻ h ⁺	Flower-like nanosphere	Multilayer	2020	106
α-Fe ₂ O ₃ /ZnFe ₂ O ₄ @Ti ₃ C ₂	Rhodamine B (RhB)	(Rate constants) 0.02686 (RhB) (Removal rate)	20 mg catalyst + 100 mL 10 mg L ⁻¹ substrate, 30 min dark adsorption	300 W Xe lamp (λ > 400 nm)	•OH •O ₂ ⁻	α-Fe ₂ O ₃ /ZnFe ₂ O ₄ nanoparticles/Ti ₃ C ₂ nanosheets	Multilayer	2019	107
Cr(vi)	Cr(vi)	Light off: about 70% in 90 min Light on: about 90% in 90 min			•OH h ⁺				

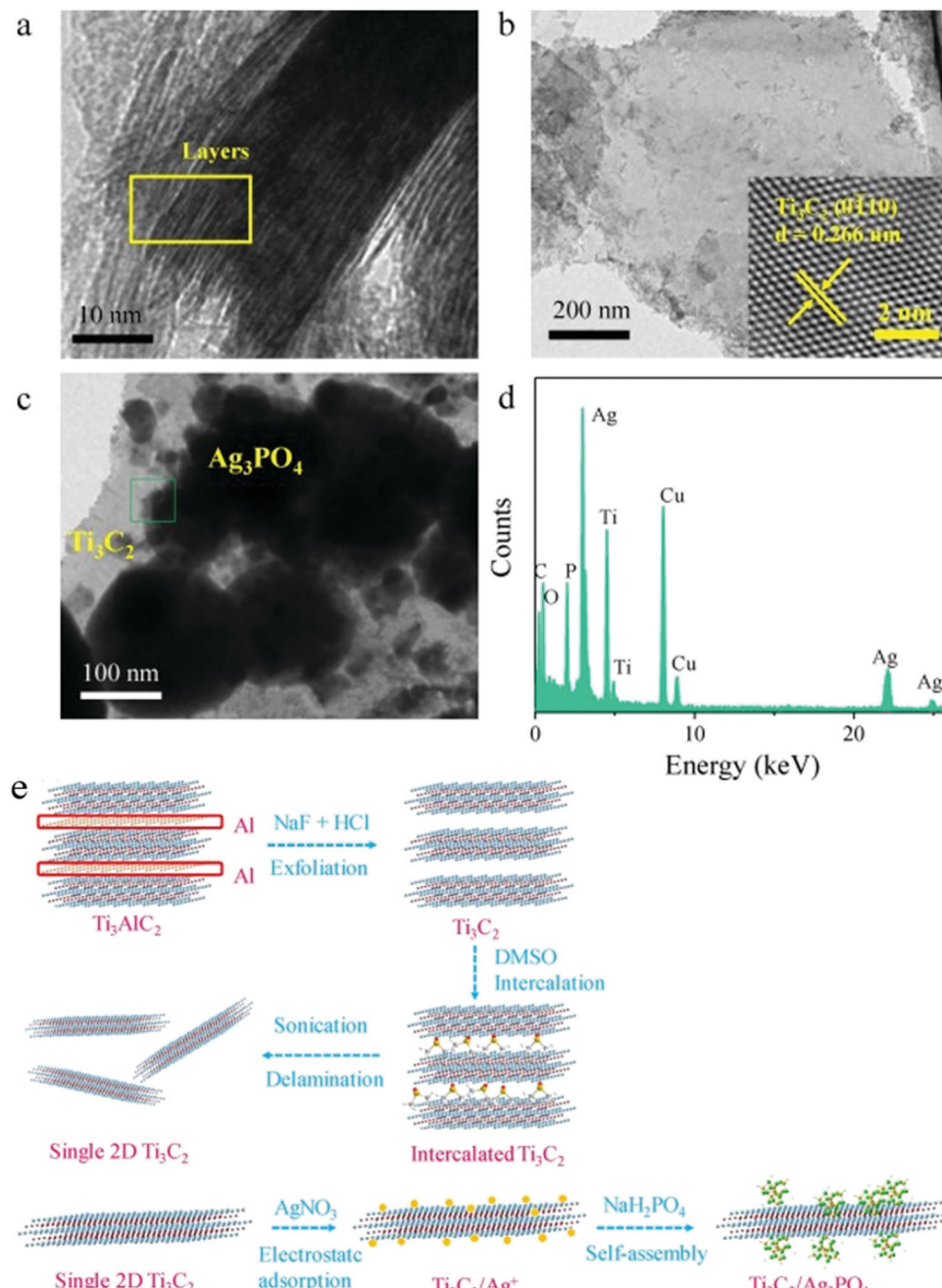


Fig. 19 TEM images of (a) bulk Ti_3C_2 , (b) single Ti_3C_2 sheet, (c) $\text{Ag}_3\text{PO}_4/\text{Ti}_3\text{C}_2$ composite. (d) EDX spectra of the $\text{Ag}_3\text{PO}_4/\text{Ti}_3\text{C}_2$ composite and (e) the schematic representation of single 2D Ti_3C_2 sheets and $\text{Ag}_3\text{PO}_4/\text{Ti}_3\text{C}_2$ synthesis.⁸⁷

needs to be explored. As is known to all, the structure of pure $\text{Ti}_3\text{C}_2\text{T}_x$ is not stable in both air and water. In air, the fresh-etched surface groups (such as $-\text{OH}$ and $-\text{F}$) can be replaced by oxygen termination after being exposed to air for a period of time; in water, $\text{Ti}_3\text{C}_2\text{T}_x$ can even be oxidized after being replaced for 21 days in room temperature.¹⁰⁸ Thus, it needs to be explored more whether the structure of $\text{Ti}_3\text{C}_2\text{T}_x$ is changed during the photocatalytic reaction and if it does, how it changes.

During photocatalytic CO_2 RR, although both monolayer-structured and multilayer-structured $\text{Ti}_3\text{C}_2\text{T}_x$ exhibit high

performance, isotope detection shows that some carbon resources come from CO_2 molecular; thus, there are still some ambiguities and other possibilities. For example, the valence state of ‘‘C’’ in $\text{Ti}_3\text{C}_2\text{T}_x$ is mostly ‘‘−4’’, which makes it possible for CO_2 to react with $\text{Ti}_3\text{C}_2\text{T}_x$ in order to form the CO as product; this pathway involves redox reaction rather than catalysis.

This, in all, the mechanism needs to be explored more, both during the photocatalytic reaction and the oxidation of $\text{Ti}_3\text{C}_2\text{T}_x$ itself.



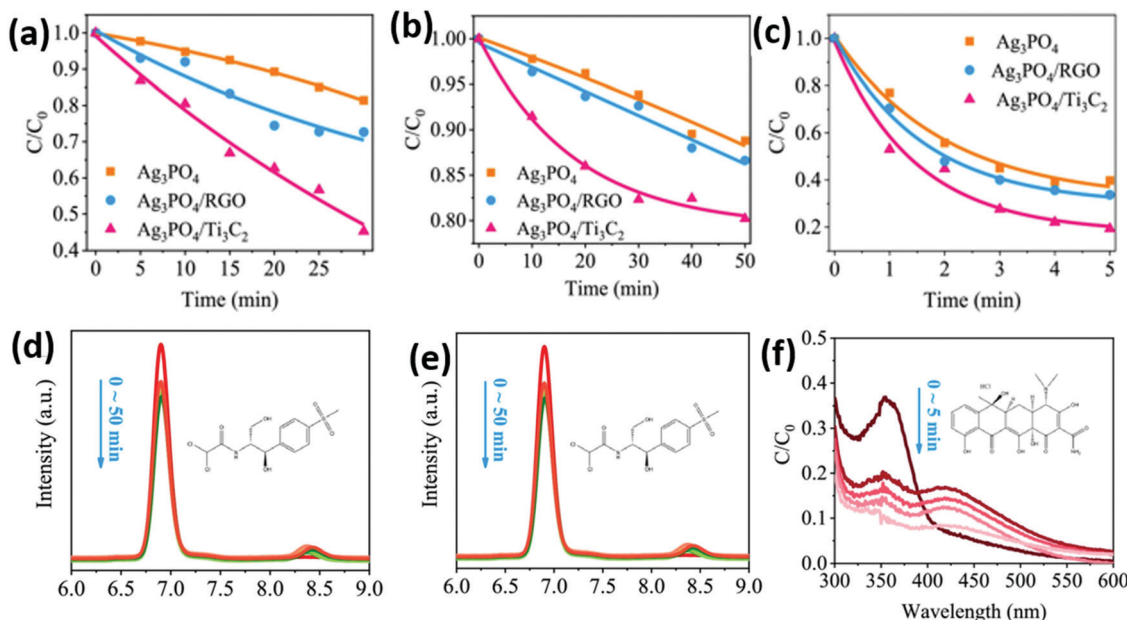


Fig. 20 Photocatalytic degradation of various pollutants by the as-prepared catalysts. (a) CPL, (b) TPL, and (c) TC-H degradation efficiency in the presence of the as-prepared catalysts under visible light irradiation ($\lambda > 420$ nm). HPLC chromatogram of (d) CPL and (e) TPL under different degradation times using the as-prepared catalysts. (f) UV-vis absorption spectra of TC-H under different degradation times using different catalysts.⁸⁷

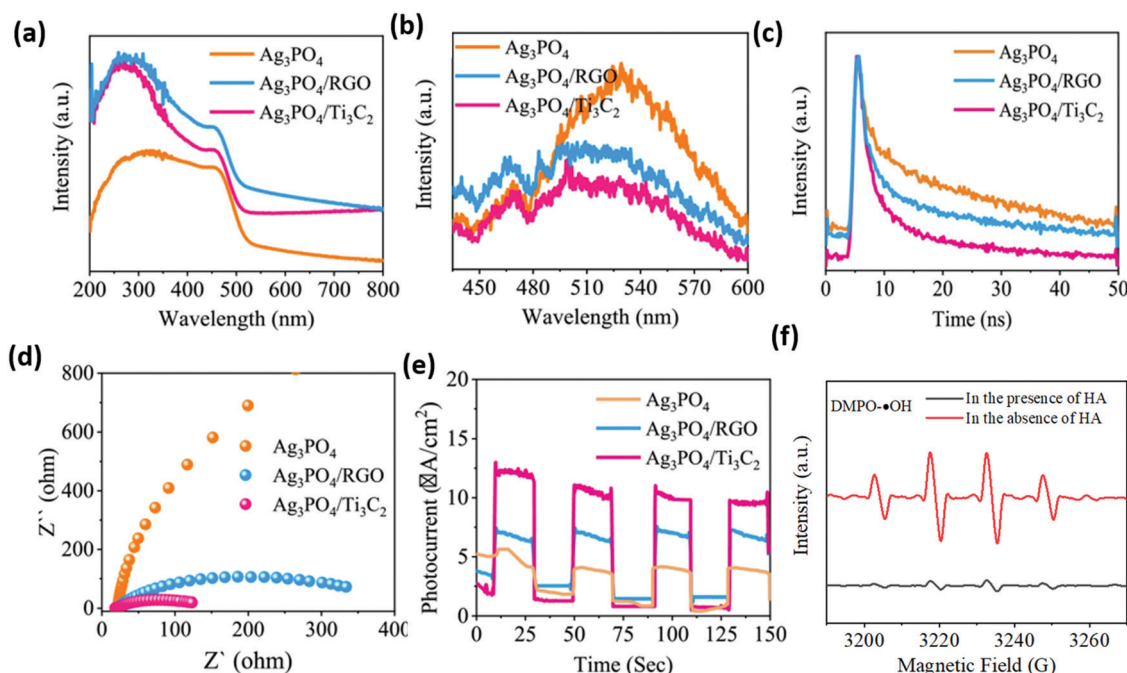


Fig. 21 UV-vis diffuse reflectance spectra (a), PL spectra (b), time-resolved PL decay spectra (c), EIS Nyquist plots (d), transient photocurrent responses (e) of the as-prepared catalysts, and DMPO spin-trapping ESR spectra for DMPO-•OH in the Ag₃PO₄/Ti₃C₂ system in the presence or absence of HA.⁸⁷

5.2.2 Development direction. The application of Ti₃C₂T_x in photocatalysis is meaningful not just because it obviously promotes the reaction but also due to its applications in other

new two-dimensional materials. For further applications, the following directions are necessary: to explore new methods of preparation to get structurally-stable Ti₃C₂T_x; to explore easier

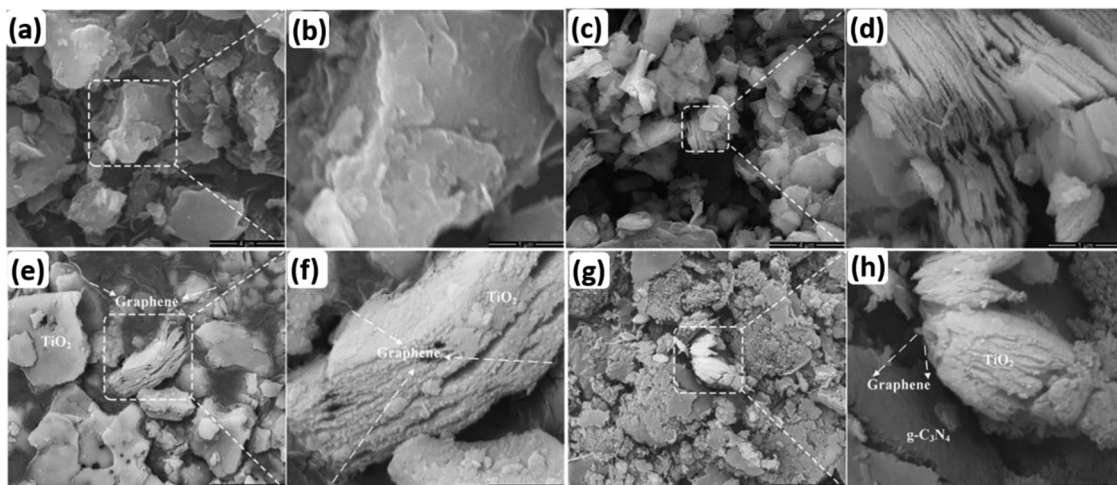


Fig. 22 SEM images of C_3N_4 (a and b), Ti_3C_2 (c and d), heated Ti_3C_2 (e and f), and graphene layers anchored $\text{TiO}_2/\text{g-C}_3\text{N}_4$ (g and h).¹⁰⁵

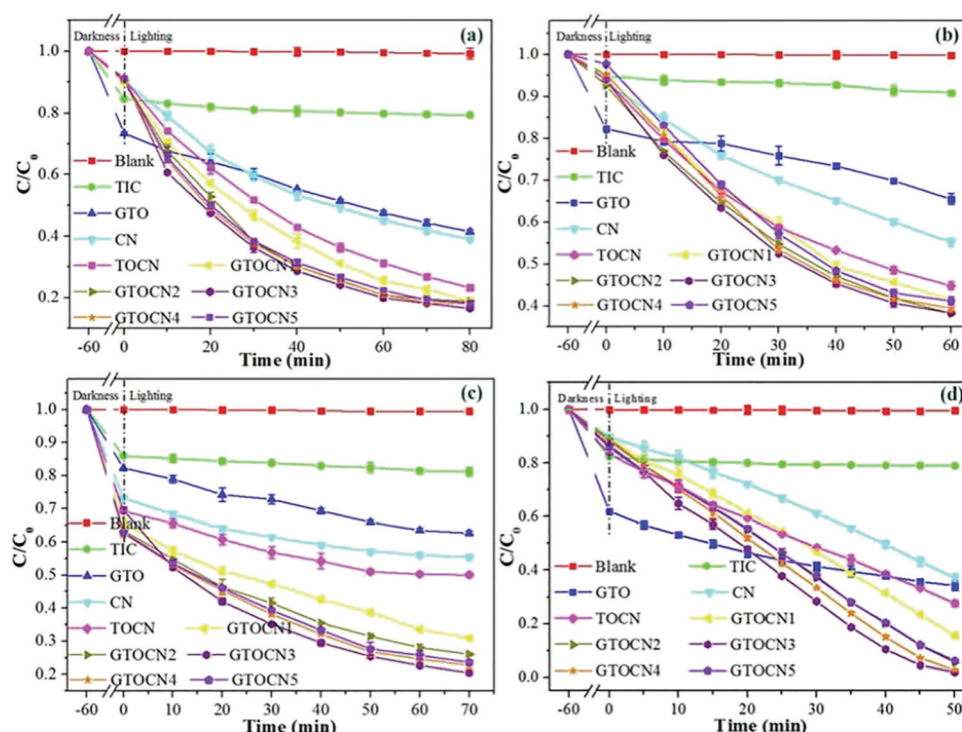


Fig. 23 The photocatalytic degradation performance of TC (a), CIP (b), BPA (c), and RhB (d) by photocatalysts under visible light irradiation.¹⁰⁵

methods of preparation to get monolayered $\text{Ti}_3\text{C}_2\text{T}_x$; to explore more effective combination between $\text{Ti}_3\text{C}_2\text{T}_x$ and the base photocatalyst; to explore methods of regulating the surface groups and interlayer groups; to explore other application in the MXene family; to explore the mechanism.

$\text{Ti}_3\text{C}_2\text{T}_x$ is the earliest material in the MXene family; thus, the improvement of its application in photocatalysis represents a great significance for the application of the whole family.

Conflicts of interest

There are no conflicts to declare.

Acknowledgements

This work was supported by the National Natural Science Foundation of China (No. 51702270 and 51872147), the 111 Project (D20015), the Program for Innovative Research Team of



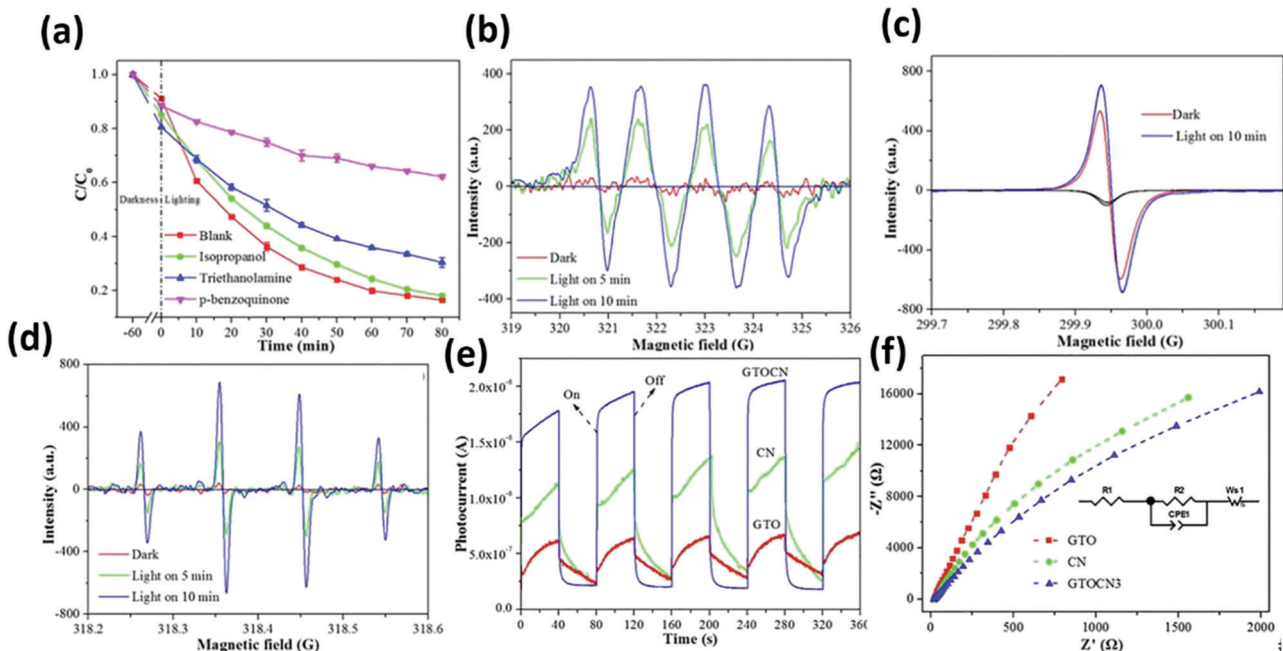


Fig. 24 Trapping experiment for the photocatalytic degradation of TC over GTOCN3 (a); ESR spectra of CNTOC3 for (b) DMPO-•O₂⁻, (c) TEMPO-h⁺, (d) DMPO-•OH in the dark and under visible light irradiation, I-T curves under visible light irradiation (e) and the EIS response (f) of the samples.¹⁰⁵

Science and Technology in the University of Henan Province (19IRTSTHN025), PetroChina Innovation Foundation (No. 2018D-5007-0604), and Sichuan Science and Technology Program (No. 2020JDJQ0057).

References

- 1 J. Mao, Z. Liu and Z. Ren, Size effect in thermoelectric materials, *npj Quantum Mater.*, 2016, **1**(1), 16028.
- 2 X. Feng, G. Hu and J. Hu, Solution-phase synthesis of metal and/or semiconductor homojunction/heterojunction nanomaterials, *Nanoscale*, 2011, **3**(5), 2099–2117.
- 3 S. Zhang, S. Guo, Z. Chen, Y. Wang, H. Gao, J. Gomez-Herrero, P. Ares, F. Zamora, Z. Zhu and H. Zeng, Recent progress in 2D group-VA semiconductors: from theory to experiment, *Chem. Soc. Rev.*, 2018, **47**(3), 982–1021.
- 4 M. Naguib, M. Kurtoglu, V. Presser, J. Lu, J. Niu, M. Heon, L. Hultman, Y. Gogotsi and M. W. Barsoum, Two-dimensional nanocrystals produced by exfoliation of Ti₃AlC₂, *Adv. Mater.*, 2011, **23**(37), 4248–4253.
- 5 N. K. Chaudhari, H. Jin, B. Kim, D. San Baek, S. H. Joo and K. Lee, MXene: an emerging two-dimensional material for future energy conversion and storage applications, *J. Mater. Chem. A*, 2017, **5**(47), 24564–24579.
- 6 Y. Zhang, L. Wang, N. Zhang and Z. Zhou, Adsorptive environmental applications of MXene nanomaterials: a review, *RSC Adv.*, 2018, **8**(36), 19895–19905.
- 7 K. Huang, Z. Li, J. Lin, G. Han and P. Huang, Two-dimensional transition metal carbides and nitrides (MXenes) for biomedical applications, *Chem. Soc. Rev.*, 2018, **47**(14), 5109–5124.
- 8 B. Anasori, M. R. Lukatskaya and Y. Gogotsi, 2D metal carbides and nitrides (MXenes) for energy storage, *Nat. Rev. Mater.*, 2017, **2**(2), 16098.
- 9 T. Deng, J. Sun, P. Tai, Y. Wang, L. Zhang, H. Chang, Z. Wang, L. Niu, Y. Sheng, D. Xue, Q. Huang, Y. Zhou, P. Song and J. Li, Ti₃AlC₂, a candidate structural material for innovative nuclear energy system: the microstructure phase transformation and defect evolution induced by energetic heavy-ion irradiation, *Acta Mater.*, 2020, **189**, 188–203.
- 10 J. Halim, M. R. Lukatskaya, K. M. Cook, J. Lu, C. R. Smith, L. A. Naslund, S. J. May, L. Hultman, Y. Gogotsi, P. Eklund and M. W. Barsoum, Transparent conductive two-dimensional titanium carbide epitaxial thin films, *Chem. Mater.*, 2014, **26**(7), 2374–2381.
- 11 A. Hu, J. Yu, H. Zhao, H. Zhang and W. Li, One-step synthesis for cations intercalation of two-dimensional carbide crystal Ti₃C₂ MXene, *Appl. Surf. Sci.*, 2020, **505**, 144538.
- 12 M. Ghidiu, M. R. Lukatskaya, M. Q. Zhao, Y. Gogotsi and M. W. Barsoum, Conductive two-dimensional titanium carbide ‘clay’ with high volumetric capacitance, *Nature*, 2014, **516**(7529), 78–81.
- 13 M. R. Lukatskaya, O. Mashtalir, C. E. Ren, Y. Dall'Agnese, P. Rozier, P. L. Taberna, M. Naguib, P. Simon, M. W. Barsoum and Y. Gogotsi, Cation intercalation and high volumetric capacitance of two-dimensional titanium carbide, *Science*, 2013, **341**(6153), 1502–1505.
- 14 L. H. Karlsson, J. Birch, J. Halim, M. W. Barsoum and P. O. Persson, Atomically resolved structural and chemical investigation of single MXene sheets, *Nano Lett.*, 2015, **15**(8), 4955–4960.



15 D. Magne, V. Mauchamp, S. Celerier, P. Chartier and T. Cabioch, Site-projected electronic structure of two-dimensional Ti_3C_2 MXene: the role of the surface functionalization groups, *Phys. Chem. Chem. Phys.*, 2016, **18**(45), 30946–30953.

16 H. W. Wang, M. Naguib, K. Page, D. J. Wesolowski and Y. Gogotsi, Resolving the structure of $Ti_3C_2T_x$ MXenes through multilevel structural modeling of the atomic pair distribution function, *Chem. Mater.*, 2016, **28**(1), 349–359.

17 K. J. Harris, M. Bugnet, M. Naguib, M. W. Barsoum and G. R. Goward, Direct measurement of surface termination groups and their connectivity in the 2D MXene V_2CT_x using NMR spectroscopy, *J. Phys. Chem. C*, 2015, **119**(24), 13713–13720.

18 M. A. Hope, A. C. Forse, K. J. Griffith, M. R. Lukatskaya, M. Ghidiu, Y. Gogotsi and C. P. Grey, NMR reveals the surface functionalisation of Ti_3C_2 MXene, *Phys. Chem. Chem. Phys.*, 2016, **18**(7), 5099–5102.

19 Q. Xue, H. Zhang, M. Zhu, Z. Pei, H. Li, Z. Wang, Y. Huang, Y. Huang, Q. Deng, J. Zhou, S. Du, Q. Huang and C. Zhi, Photoluminescent Ti_3C_2 MXene quantum dots for multi-color cellular imaging, *Adv. Mater.*, 2017, **29**(15), 1604847.

20 D. Er, J. Li, M. Naguib, Y. Gogotsi and V. B. Shenoy, Ti_3C_2 MXene as a high capacity electrode material for metal (Li, Na, K, Ca) ion batteries, *ACS Appl. Mater. Interfaces*, 2014, **6**(14), 11173–11179.

21 Q. Tang, Z. Zhou and P. Shen, Are MXenes promising anode materials for Li ion batteries? Computational studies on electronic properties and Li storage capability of Ti_3C_2 and $Ti_3C_2X_2$ (X = F, OH) monolayer, *J. Am. Chem. Soc.*, 2012, **134**(40), 16909–16916.

22 Q. Hu, D. Sun, Q. Wu, H. Wang, L. Wang, B. Liu, A. Zhou and J. He, MXene: a new family of promising hydrogen storage medium, *J. Phys. Chem. A*, 2013, **117**(51), 14253–14260.

23 Y. Xie, Y. Dall'Agnese, M. Naguib, Y. Gogotsi, M. W. Barsoum, H. L. L. Zhuang and P. R. C. Kent, Prediction and characterization of MXene nanosheet anodes for non-lithium-ion batteries, *ACS Nano*, 2014, **8**(9), 9606–9615.

24 C. Eames and M. S. Islam, Ion intercalation into two-dimensional transition-metal carbides: global screening for new high-capacity battery materials, *J. Am. Chem. Soc.*, 2014, **136**(46), 16270–16276.

25 H. Pan, Ultra-high electrochemical catalytic activity of MXenes, *Sci. Rep.*, 2016, **6**, 32531.

26 M. Q. Zhao, C. E. Ren, Z. Ling, M. R. Lukatskaya, C. F. Zhang, K. L. Van Aken, M. W. Barsoum and Y. Gogotsi, Flexible MXene/Carbon nanotube composite paper with high volumetric capacitance, *Adv. Mater.*, 2015, **27**(2), 339–345.

27 Z. Guo, J. Zhou, L. Zhu and Z. Sun, MXene: a promising photocatalyst for water splitting, *J. Mater. Chem. A*, 2016, **4**(29), 11446–11452.

28 M. Q. Zhao, C. E. Ren, Z. Ling, M. R. Lukatskaya, C. F. Zhang, K. L. Van Aken, M. W. Barsoum and Y. Gogotsi, Flexible MXene/Carbon nanotube composite paper with high volumetric capacitance, *Adv. Mater.*, 2015, **27**(2), 339–345.

29 G. Gao, A. P. O'Mullane and A. Du, 2D MXenes: A new family of promising catalysts for the hydrogen evolution reaction, *ACS Catal.*, 2016, **7**(1), 494–500.

30 J. Ran, G. Gao, F.-T. Li, T.-Y. Ma, A. Du and S.-Z. Qiao, Ti_3C_2 MXene co-catalyst on metal sulfide photo-absorbers for enhanced visible-light photocatalytic hydrogen production, *Nat. Commun.*, 2017, **8**(1), 13907.

31 M. Naguib, O. Mashtalir, M. R. Lukatskaya, B. Dyatkin, C. Zhang, V. Presser, Y. Gogotsi and M. W. Barsoum, One-step synthesis of nanocrystalline transition metal oxides on thin sheets of disordered graphitic carbon by oxidation of MXenes, *Chem. Commun.*, 2014, **50**(56), 7420–7423.

32 X. Han, L. An, Y. Hu, Y. Li, C. Hou, H. Wang and Q. Zhang, Ti_3C_2 MXene-derived carbon-doped TiO_2 coupled with g - C_3N_4 as the visible-light photocatalysts for photocatalytic H_2 generation, *Appl. Catal., B*, 2020, **265**, 118539.

33 X. Sang, Y. Xie, M. W. Lin, M. Alhabeb, K. L. Van Aken, Y. Gogotsi, P. R. C. Kent, K. Xiao and R. R. Unocic, Atomic defects in monolayer titanium carbide ($Ti_3C_2T_x$) MXene, *ACS Nano*, 2016, **10**(10), 9193–9200.

34 W. Zhou, X. Zou, S. Najmaei, Z. Liu, Y. Shi, J. Kong, J. Lou, P. M. Ajayan, B. I. Yakobson and J. C. Idrobo, Intrinsic structural defects in monolayer molybdenum disulfide, *Nano Lett.*, 2013, **13**(6), 2615–2622.

35 M. H. Gass, U. Bangert, A. L. Bleloch, P. Wang, R. R. Nair and A. K. Geim, Free-standing graphene at atomic resolution, *Nat. Nanotechnol.*, 2008, **3**(11), 676–681.

36 K. Takanabe, Photocatalytic Water Splitting: Quantitative Approaches toward Photocatalyst by Design, *ACS Catal.*, 2017, **7**(11), 8006–8022.

37 J. Ran, J. Zhang, J. Yu, M. Jaroniec and S. Z. Qiao, Earth-abundant cocatalysts for semiconductor-based photocatalytic water splitting, *Chem. Soc. Rev.*, 2014, **43**(22), 7787–7812.

38 S. S. Chen, T. Takata and K. Domen, Particulate photocatalysts for overall water splitting, *Nat. Rev. Mater.*, 2017, **2**(10), 17050.

39 A. Kudo and Y. Miseki, Heterogeneous photocatalyst materials for water splitting, *Chem. Soc. Rev.*, 2009, **38**(1), 253–278.

40 Y. Jiao, Y. Zheng, M. Jaroniec and S. Z. Qiao, Design of electrocatalysts for oxygen- and hydrogen-involving energy conversion reactions, *Chem. Soc. Rev.*, 2015, **44**(8), 2060–2086.

41 J. K. Norskov, T. Bligaard, J. Rossmeisl and C. H. Christensen, Towards the computational design of solid catalysts, *Nat. Chem.*, 2009, **1**(1), 37–46.

42 J. K. Nørskov, T. Bligaard, A. Logadottir, J. R. Kitchin, J. G. Chen, S. Pandelov and U. Stimming, Trends in the exchange current for hydrogen evolution, *J. Electrochem. Soc.*, 2005, **152**(3), J23.

43 H. Berit, G. H. Poul, B. Jacob, P. J. Kristina, H. N. Jane, H. Sebastina, C. Ib and K. N. Jens, Biomimetic hydrogen evolution: MoS_2 nanoparticles as catalyst for hydrogen evolution, *J. Am. Chem. Soc.*, 2005, **127**(15), 5308–5309.

44 W. Yuan, L. Cheng, Y. Zhang, H. Wu, S. Lv, L. Chai, X. Guo and L. Zheng, 2D-layered Carbon/ TiO_2 hybrids derived



from Ti_3C_2 MXenes for photocatalytic hydrogen evolution under visible light irradiation, *Adv. Mater. Interfaces*, 2017, **4**(20), 1700577.

45 H. Wang, R. Peng, Z. D. Hood, M. Naguib, S. P. Adhikari and Z. Wu, Titania composites with 2D transition metal carbides as photocatalysts for hydrogen production under visible-light irradiation, *ChemSusChem*, 2016, **9**(12), 1490–1497.

46 X. An, W. Wang, J. Wang, H. Duan, J. Shi and X. Yu, The synergistic effects of Ti_3C_2 MXene and Pt as co-catalysts for highly efficient photocatalytic hydrogen evolution over $g\text{-}C_3N_4$. *Phys. Chem. Chem. Phys.*, 2018, **20**(16), 11405–11411.

47 W. Yuan, L. Cheng, Y. An, S. Lv, H. Wu, X. Fan, Y. Zhang, X. Guo and J. Tang, Laminated hybrid junction of sulfur-doped TiO_2 and a carbon substrate derived from Ti_3C_2 MXenes: toward highly visible light-driven photocatalytic hydrogen evolution, *Adv. Sci.*, 2018, **5**(6), 1700870.

48 Y. Li, X. Deng, J. Tian, Z. Liang and H. Cui, Ti_3C_2 MXene-derived Ti_3C_2/TiO_2 nanoflowers for noble-metal-free photocatalytic overall water splitting. *Appl. Mater. Today*, 2018, **13**, 217–227.

49 H. Wang, Y. Sun, Y. Wu, W. Tu, S. Wu, X. Yuan, G. Zeng, Z. J. Xu, S. Li and J. W. Chew, Electrical promotion of spatially photoinduced charge separation *via* interfacial-built-in quasi-alloying effect in hierarchical $Zn_2In_2S_5/Ti_3C_2(O, OH)_x$ hybrids toward efficient photocatalytic hydrogen evolution and environmental remediation, *Appl. Catal., B*, 2019, **245**, 290–301.

50 M. Zhang, J. Qin, S. Rajendran, X. Zhang and R. Liu, Heterostructured d- $Ti_3C_2/TiO_2/g\text{-}C_3N_4$ nanocomposites with enhanced visible-light photocatalytic hydrogen production activity, *ChemSusChem*, 2018, **11**(24), 4226–4236.

51 L. Tie, S. Yang, C. Yu, H. Chen, Y. Liu, S. Dong, J. Sun and J. Sun, In situ decoration of ZnS nanoparticles with Ti_3C_2 MXene nanosheets for efficient photocatalytic hydrogen evolution, *J. Colloid Interface Sci.*, 2019, **545**, 63–70.

52 R. Xiao, C. Zhao, Z. Zou, Z. Chen, L. Tian, H. Xu, H. Tang, Q. Liu, Z. Lin and X. Yang, In situ fabrication of 1D CdS nanorod/2D Ti_3C_2 MXene nanosheet Schottky heterojunction toward enhanced photocatalytic hydrogen evolution, *Appl. Catal., B*, 2020, **268**, 118382.

53 Y. Zhuang, Y. Liu and X. Meng, Fabrication of TiO_2 nanofibers/MXene Ti_3C_2 nanocomposites for photocatalytic H_2 evolution by electrostatic self-assembly, *Appl. Surf. Sci.*, 2019, **496**, 143647.

54 T. Su, Z. D. Hood, M. Naguib, L. Bai, S. Luo, C. M. Rouleau, I. N. Ivanov, H. Ji, Z. Qin and Z. Wu, Monolayer Ti_3C_2Tx as an effective co-catalyst for enhanced photocatalytic hydrogen production over TiO_2 , *ACS Appl. Energy Mater.*, 2019, **2**(7), 4640–4651.

55 J. Zhang, C. Xing and F. Shi, MoS_2/Ti_3C_2 heterostructure for efficient visible-light photocatalytic hydrogen generation, *Int. J. Hydrogen Energy*, 2020, **45**(11), 6291–6301.

56 P. Lin, J. Shen, X. Yu, Q. Liu, D. Li and H. Tang, Construction of Ti_3C_2 MXene/O-doped $g\text{-}C_3N_4$ 2D–2D Schottky junction for enhanced photocatalytic hydrogen evolution, *Ceram. Int.*, 2019, **45**(18), 24656–24663.

57 L. Cheng, Q. Chen, J. Li and H. Liu, Boosting the photocatalytic activity of $CdLa_2S_4$ for hydrogen production using Ti_3C_2 MXene as a co-catalyst, *Appl. Catal., B*, 2020, **267**, 118379.

58 Y. Li, L. Ding, Y. Guo, Z. Liang, H. Cui and J. Tian, Boosting the photocatalytic ability of $g\text{-}C_3N_4$ for hydrogen production by Ti_3C_2 MXene quantum dots, *ACS Appl. Mater. Interfaces*, 2019, **11**(44), 41440–41447.

59 Y. Li, L. Ding, Z. Liang, Y. Xue, H. Cui and J. Tian, Synergetic effect of defects rich MoS_2 and Ti_3C_2 MXene as cocatalysts for enhanced photocatalytic H_2 production activity of TiO_2 , *Chem. Eng. J.*, 2020, **383**, 123178.

60 P. Tian, X. He, L. Zhao, W. Li, W. Fang, H. Chen, F. Zhang, Z. Huang and H. Wang, Ti_3C_2 nanosheets modified Zr-MOFs with Schottky junction for boosting photocatalytic HER performance, *Sol. Energy*, 2019, **188**, 750–759.

61 Z. Ai, K. Zhang, B. Chang, Y. Shao, L. Zhang, Y. Wu and X. Hao, Construction of $CdS@Ti_3C_2@CoO$ hierarchical tandem p–n heterojunction for boosting photocatalytic hydrogen production in pure water, *Chem. Eng. J.*, 2020, **383**, 123130.

62 J.-H. Zhao, L.-W. Liu, K. Li, T. Li and F.-T. Liu, Conductive Ti_3C_2 and MOF-derived CoS_x boosting the photocatalytic hydrogen production activity of TiO_2 , *CrystEngComm*, 2019, **21**(14), 2416–2421.

63 Z. Ai, Y. Shao, B. Chang, B. Huang, Y. Wu and X. Hao, Effective orientation control of photogenerated carrier separation *via* rational design of a $Ti_3C_2(TiO_2)@CdS/MoS_2$ photocatalytic system, *Appl. Catal., B*, 2019, **242**, 202–208.

64 Y. Li, Z. Yin, G. Ji, Z. Liang, Y. Xue, Y. Guo, J. Tian, X. Wang and H. Cui, 2D/2D/2D heterojunction of Ti_3C_2 MXene/ MoS_2 nanosheets/ TiO_2 nanosheets with exposed (001) facets toward enhanced photocatalytic hydrogen production activity, *Appl. Catal., B*, 2019, **246**, 12–20.

65 J. Li, L. Zhao, S. Wang, J. Li, G. Wang and J. Wang, In situ fabrication of 2D/3D $g\text{-}C_3N_4/Ti_3C_2$ (MXene) heterojunction for efficient visible-light photocatalytic hydrogen evolution, *Appl. Surf. Sci.*, 2020, **515**, 145922.

66 J. Zhang, M. Liu, Y. Wang and F. Shi, $Au/MoS_2/Ti_3C_2$ composite catalyst for efficient photocatalytic hydrogen evolution, *CrystEngComm*, 2020, **22**(21), 3683–3691.

67 T. Su, Z. D. Hood, M. Naguib, L. Bai, S. Luo, C. M. Rouleau, I. N. Ivanov, H. Ji, Z. Qin and Z. Wu, 2D/2D heterojunction of $Ti_3C_2/g\text{-}C_3N_4$ nanosheets for enhanced photocatalytic hydrogen evolution, *Nanoscale*, 2019, **11**(17), 8138–8149.

68 J. Yin, F. Zhan, T. Jiao, W. Wang, G. Zhang, J. Jiao, G. Jiang, Q. Zhang, J. Gu and Q. Peng, Facile preparation of self-assembled MXene@Au@CdS nanocomposite with enhanced photocatalytic hydrogen production activity, *Sci. China Mater.*, 2020, **63**(11), 2228–2238.

69 Z. Yao, H. Sun, H. Sui and X. Liu, Construction of BPQDs/ $Ti_3C_2@TiO_2$ composites with favorable charge transfer channels for enhanced photocatalytic activity under visible light irradiation, *Nanomater.*, 2020, **10**(3), 452.



70 J. Liu, H.-B. Zhang, R. Sun, Y. Liu, Z. Liu, A. Zhou and Z.-Z. Yu, Hydrophobic, flexible, and lightweight MXene foams for high-performance electromagnetic-interference shielding, *Adv. Mater.*, 2017, **29**(38), 1702367.

71 Y. Chen, G. Jia, Y. Hu, G. Fan, Y. H. Tsang, Z. Li and Z. Zou, Two-dimensional nanomaterials for photocatalytic CO₂ reduction to solar fuels, *Sustainable Energy Fuels*, 2017, **1**(9), 1875–1898.

72 J. Fu, K. Jiang, X. Qiu, J. Yu and M. Liu, Product selectivity of photocatalytic CO₂ reduction reactions, *Mater. Today*, 2020, **32**, 222–243.

73 K. Li, B. Peng and T. Peng, Recent advances in heterogeneous photocatalytic CO₂ conversion to solar fuels, *ACS Catal.*, 2016, **6**(11), 7485–7527.

74 J. L. White, M. F. Baruch, J. E. Pander III, Y. Hu, I. C. Fortmeyer, J. E. Park, T. Zhang, K. Liao, J. Gu, Y. Yan, T. W. Shaw, E. Abelev and A. B. Bocarsly, Light-driven heterogeneous reduction of carbon dioxide: photocatalysts and photoelectrodes, *Chem. Rev.*, 2015, **115**(23), 12888–12935.

75 X. Zhang, Z. Zhang, J. Li, X. Zhao, D. Wu and Z. Zhou, Ti₂CO₂ MXene: a highly active and selective photocatalyst for CO₂ reduction, *J. Mater. Chem. A*, 2017, **5**(25), 12899–12903.

76 H. He, P. Zapol and L. A. Curtiss, Computational screening of dopants for photocatalytic two-electron reduction of CO₂ on anatase (101) surfaces, *Energy Environ. Sci.*, 2012, **5**(3), 6196–6205.

77 Y. Ji and Y. Luo, Theoretical study on the mechanism of photoreduction of CO₂ to CH₄ on the anatase TiO₂(101) surface, *ACS Catal.*, 2016, **6**(3), 2018–2025.

78 Y. Ji and Y. Luo, New mechanism for photocatalytic reduction of CO₂ on the anatase TiO₂(101) surface: the essential role of oxygen vacancy, *J. Am. Chem. Soc.*, 2016, **138**(49), 15896–15902.

79 C. Yang, Q. Tan, Q. Li, J. Zhou, J. Fan, B. Li, J. Sun and K. Lv, 2D/2D Ti₃C₂ MXene/g-C₃N₄ nanosheets heterojunction for high efficient CO₂ reduction photocatalyst: Dual effects of urea, *Appl. Catal. B*, 2020, **268**, 118738.

80 Q. Tang, Z. Sun, S. Deng, H. Wang and Z. Wu, Decorating g-C₃N₄ with alkalinized Ti₃C₂ MXene for promoted photocatalytic CO₂ reduction performance, *J. Colloid Interface Sci.*, 2020, **564**, 406–417.

81 J. Low, L. Zhang, T. Tong, B. Shen and J. Yu, TiO₂/MXene Ti₃C₂ composite with excellent photocatalytic CO₂ reduction activity, *J. Catal.*, 2018, **361**, 255–266.

82 S. Cao, B. Shen, T. Tong, J. Fu and J. Yu, 2D/2D heterojunction of ultrathin MXene/Bi₂WO₆ nanosheets for improved photocatalytic CO₂ reduction, *Adv. Funct. Mater.*, 2018, **28**(21), 1800136.

83 F. He, B. Zhu, B. Cheng, J. Yu, W. Ho and W. Macyk, 2D/2D/0D TiO₂/C₃N₄/Ti₃C₂ MXene composite S-scheme photocatalyst with enhanced CO₂ reduction activity, *Appl. Catal. B*, 2020, **272**, 119006.

84 J. Halim, K. M. Cook, M. Naguib, P. Eklund, Y. Gogotsi, J. Rosen and M. W. Barsoum, X-ray photoelectron spectroscopy of select multi-layered transition metal carbides (MXenes), *Appl. Surf. Sci.*, 2016, **362**, 406–417.

85 L. Liang, F. Lei, S. Gao, Y. Sun, X. Jiao, J. Wu, S. Qamar and Y. Xie, Single unit cell bismuth tungstate layers realizing robust solar CO₂ reduction to methanol, *Angew. Chem., Int. Ed.*, 2015, **54**(47), 13971–13974.

86 H. Lin, X. Wang, L. Yu, Y. Chen and J. Shi, Two-dimensional ultrathin MXene ceramic nanosheets for photothermal conversion, *Nano Lett.*, 2017, **17**(1), 384–391.

87 T. Cai, L. Wang, Y. Liu, S. Zhang, W. Dong, H. Chen, X. Yi, J. Yuan, X. Xia, C. Liu and S. Luo, Ag₃PO₄/Ti₃C₂ MXene interface materials as a Schottky catalyst with enhanced photocatalytic activities and anti-photocorrosion performance, *Appl. Catal. B*, 2018, **239**, 545–554.

88 X. Zhao, M. Liu, Y. Chen, B. Hou, N. Zhang, B. Chen, N. Yang, K. Chen, J. Li and L. An, Fabrication of layered Ti₃C₂ with an accordion-like structure as a potential cathode material for high performance lithium–sulfur batteries, *J. Mater. Chem. A*, 2015, **3**(15), 7870–7876.

89 J. Qian, A. Yuan, C. Yao, J. Liu, B. Li, F. Xi and X. Dong, Highly Efficient Photo-Reduction of p-nitrophenol by protonated graphitic carbon nitride nanosheets, *ChemCatChem*, 2018, **10**(20), 4747–4754.

90 M. R. Hoffmann, S. T. Martin and W. Choi, Environmental Applications of semiconductor photocatalysis, *Chem. Rev.*, 1995, **95**(1), 69–96.

91 S. Dong, J. Feng, M. Fan, Y. Pi, L. Hu, X. Han, M. Liu, J. Sun and J. Sun, Recent developments in heterogeneous photocatalytic water treatment using visible light-responsive photocatalysts: a review, *RSC Adv.*, 2015, **5**(19), 14610–14630.

92 W. Guo, F. Zhang, C. Lin and Z. L. Wang, Direct growth of TiO₂ nanosheet arrays on carbon fibers for highly efficient photocatalytic degradation of methyl orange, *Adv. Mater.*, 2012, **24**(35), 4761–4764.

93 G. Xi and J. Ye, Synthesis of bismuth vanadate nanoplates with exposed {001} facets and enhanced visible-light photocatalytic properties, *Chem. Commun.*, 2010, **46**(11), 1893–1895.

94 B. B. Adormaa, W. K. Darkwah and Y. Ao, Oxygen vacancies of the TiO₂ nano-based composite photocatalysts in visible light responsive photocatalysis, *RSC Adv.*, 2018, **8**(58), 33551–33563.

95 V. Augugliaro, M. Bellardita, V. Loddo, G. Palmisano, L. Palmisano and S. Yurdakal, Overview on oxidation mechanisms of organic compounds by TiO₂ in heterogeneous photocatalysis, *J. Photochem. Photobiol. C*, 2012, **13**(3), 224–245.

96 Y. Nosaka and A. Y. Nosaka, Generation and Detection of Reactive Oxygen Species in Photocatalysis, *Chem. Rev.*, 2017, **117**(17), 11302–11336.

97 H. Deng, Z.-j. Li, L. Wang, L.-y. Yuan, J.-h. Lan, Z.-y. Chang, Z.-f. Chai, W.-q. Shi and Nanolayered Ti₃C₂, and SrTiO₃ composites for photocatalytic reduction and removal of uranium(vi), *ACS Appl. Nano Mater.*, 2019, **2**(4), 2283–2294.

98 H. Fang, Y. Pan, M. Yin and C. Pan, Enhanced photocatalytic activity and mechanism of Ti₃C₂–OH/Bi₂WO₆: Yb³⁺, Tm³⁺



towards degradation of RhB under visible and near infrared light irradiation, *Mater. Res. Bull.*, 2020, **121**, 110618.

99 S. Jiao and L. Liu, Friction-induced enhancements for photocatalytic degradation of $\text{MoS}_2@\text{Ti}_3\text{C}_2$ nanohybrid, *Ind. Eng. Chem. Res.*, 2019, **58**(39), 18141–18148.

100 K. Li, X. Lu, Y. Zhang, K. Liu, Y. Huang and H. Liu, $\text{Bi}_3\text{TaO}_7/\text{Ti}_3\text{C}_2$ heterojunctions for enhanced photocatalytic removal of water-borne contaminants, *Environ. Res.*, 2020, **185**, 109409.

101 N. Liu, N. Lu, H. Yu, S. Chen and X. Quan, Efficient day-night photocatalysis performance of 2D/2D Ti_3C_2 /Porous g-C₃N₄ nanolayers composite and its application in the degradation of organic pollutants, *Chemosphere*, 2020, **246**, 125760.

102 Q. Liu, X. Tan, S. Wang, F. Ma, H. Znad, Z. Shen, L. Liu and S. Liu, MXene as a non-metal charge mediator in 2D layered $\text{CdS}@\text{Ti}_3\text{C}_2@\text{TiO}_2$ composites with superior Z-scheme visible light-driven photocatalytic activity, *Environ. Sci. Nano*, 2019, **6**(10), 3158–3169.

103 C. Peng, H. Wang, H. Yu and F. Peng, (111) $\text{TiO}_{2-x}/\text{Ti}_3\text{C}_2$: Synergy of active facets, interfacial charge transfer and Ti³⁺ doping for enhance photocatalytic activity, *Mater. Res. Bull.*, 2017, **89**, 16–25.

104 C. Peng, X. Yang, Y. Li, H. Yu, H. Wang and F. Peng, Hybrids of two-dimensional Ti_3C_2 and TiO_2 exposing {001} facets toward enhanced photocatalytic activity, *ACS Appl. Mater. Interfaces*, 2016, **8**(9), 6051–6060.

105 Z. Wu, Y. Liang, X. Yuan, D. Zou, J. Fang, L. Jiang, J. Zhang, H. Yang and Z. Xiao, MXene Ti_3C_2 derived Z-scheme photocatalyst of graphene layers anchored $\text{TiO}_2/\text{g-C}_3\text{N}_4$ for visible light photocatalytic degradation of refractory organic pollutants, *Chem. Eng. J.*, 2020, **394**, 124921.

106 Z. Yao, H. Sun, H. Sui and X. Liu, 2D/2D Heterojunction of R-scheme Ti_3C_2 MXene/ MoS_2 nanosheets for enhanced photocatalytic performance, *Nanoscale Res. Lett.*, 2020, **15**(1), 78.

107 H. Zhang, M. Li, C. Zhu, Q. Tang, P. Kang and J. Cao, Preparation of magnetic $\alpha\text{-Fe}_2\text{O}_3/\text{ZnFe}_2\text{O}_4@\text{Ti}_3\text{C}_2$ MXene with excellent photocatalytic performance, *Ceram. Int.*, 2020, **46**(1), 81–88.

108 X. Zhao, A. Vashisth, E. Prehn, W. Sun, S. A. Shah, T. Habib, Y. Chen, Z. Tan, J. L. Lutkenhaus, M. Radovic and M. J. Green, Antioxidants unlock shelf-stable $\text{Ti}_3\text{C}_2\text{T}$ (MXene) nanosheet dispersions, *Matter*, 2019, **1**(2), 513–526.

